THIRD TSUNAMI SYMPOSIUM PAPERS - II

OBJECTIVE: **The Tsunami Society** publishes this journal to increase and disseminate knowledge about tsunamis and their hazards.

DISCLAIMER: Although these articles have been technically reviewed by peers, **The Tsunami Society** is not responsible for the veracity of any statement, opinion or consequences.

Submit manuscripts of articles, notes or letters to the Editor. If an article is accepted for publication the author(s) must submit a scan ready manuscript, a Doc, TeX or a PDF file in the journal format. Issues of the journal are published electronically in PDF format. Recent journal issues are available at
http://www.sthjournal.org.

Tsunami Society members will be advised by e-mail when a new issue is available. There are no page charges or reprints for authors.

Permission to use figures, tables and brief excerpts from this journal in scientific and educational works is hereby granted provided that the source is acknowledged.

Issues of the journal from 1982 thru 2005 are available in PDF format at
http://epubs.lanl.gov/tsunami/
and on a CD-ROM from the Society to Tsunami Society members.

TIDE-TSUNAMI INTERACTIONS

Zygmunt Kowalik, Tatiana Proshutinsky,
Institute of Marine Science, University of Alaska, Fairbanks, AK, USA

Andrey Proshutinsky,
Woods Hole Oceanographic Institution, Woods Hole, MA, USA

ABSTRACT

In this paper we investigate important dynamics defining tsunami enhancement in the coastal regions and related to interaction with tides. Observations and computations of the Indian Ocean Tsunami usually show amplifications of the tsunami in the near-shore regions due to water shoaling. Additionally, numerous observations depicted quite long ringing of tsunami oscillations in the coastal regions, suggesting either local resonance or the local trapping of the tsunami energy. In the real ocean, the short-period tsunami wave rides on the longer-period tides. The question is whether these two waves can be superposed linearly for the purpose of determining the resulting sea surface height (SSH) or rather in the shallow water they interact nonlinearly, enhancing/reducing the total sea level and currents. Since the near–shore bathymetry is important for the run-up computation, Weisz and Winter (2005) demonstrated that the changes of depth caused by tides should not be neglected in tsunami run-up considerations. On the other hand, we hypothesize that much more significant effect of the tsunami-tide interaction should be observed through the tidal and tsunami currents. In order to test this hypothesis we apply a simple set of 1-D equations of motion and continuity to demonstrate the dynamics of tsunami and tide interaction in the vicinity of the shelf break for two coastal domains: shallow waters of an elongated inlet and narrow shelf typical for deep waters of the Gulf of Alaska.

1. EQUATION OF MOTION AND CONTINUITY FOR THE TSUNAMI-TIDE INTERACTION.

The tide-tsunami interaction will be investigated based on the long-wave equations of motion (Kowalik and Proshutinsky, 1994)

$$\frac{\partial u}{\partial t} + u\frac{\partial u}{\partial x} + v\frac{\partial u}{\partial y} - fv = -g\frac{\partial \zeta}{\partial x} - \frac{\partial \Omega_T}{\partial x} - \tau_x^b/\rho D \tag{1}$$

$$\frac{\partial v}{\partial t} + u\frac{\partial v}{\partial x} + v\frac{\partial v}{\partial y} + fu = -g\frac{\partial \zeta}{\partial y} - \frac{\partial \Omega_T}{\partial y} - \tau_y^b/\rho D \tag{2}$$

In these equations: x and y are coordinates directed towards East and North, respectively; velocities along these coordinates are u and v; t is time; Coriolis parameter $f = 2\Omega\sin\phi$ is a function of the Earth's angular velocity $\Omega = 7.29\times10^{-5}\,s^{-1}$ and the latitude - ϕ; ρ denotes density of the sea water; ζ is the sea level change around the mean sea level; Ω_T is the tide producing potential, and τ_x^b and τ_y^b are components of the stress at the bottom; $D = H + \zeta$ is the total depth equal to the average depth H plus the sea level variations ζ. The bottom stress is proportional to the square of the velocity:

$$\tau_x^b = \rho r u\sqrt{u^2 + v^2} \qquad \text{and} \qquad \tau_y^b = \rho r v\sqrt{u^2 + v^2} \tag{3}$$

The dimensionless friction coefficient r is taken as $r = 2.6\times10^{-3}$.
Equation of continuity for the tsunami-tide problem is formulated as,

$$\frac{\partial}{\partial t}(\zeta - \zeta_b) + \frac{\partial uD}{\partial x} + \frac{\partial vD}{\partial y} = 0 \tag{4}$$

Here, D is the total depth defined as $D = H + \zeta - \zeta_b$, ζ as before denotes the free surface change and ζ_b is the bottom deformation.
The tidal potential in eqs.1 and 2 is related to the equilibrium tides. It is given by the equilibrium surface elevation (ζ_0) as (Pugh, 1987)

$$\zeta_0 = -\frac{\Omega_T}{g} \tag{5}$$

Harmonic constituents of the equilibrium tide can be represented in the following way:
Semidiurnal species

$$\zeta_0 = K\cos^2\phi\cos(\omega t + \kappa + 2\lambda) \tag{6}$$

Here: K – amplitude (see Table 1), ϕ – latitude, ω - frequency, κ – astronomical argument, λ – longitude (east)
Diurnal species

$$\zeta_0 = K\sin 2\phi\cos(\omega t + \kappa + \lambda) \tag{7}$$

Long-period species

$$\zeta_0 = K(\frac{3}{2}\cos^2\phi - 1)\cos(\omega t + \kappa) \tag{8}$$

The amplitude factor K gives magnitude of the individual constituents in the total sea level due to equilibrium tide. The strongest constituent is M_2 with amplitude 0.24 m, the next constituent K_1 of mixed luni-solar origin has amplitude 0.14 m.

TABLE 1. PARAMETERS OF THE MAJOR TIDAL CONSTITUENTS

Name of tide	Symb	Period	Freq. (s^{-1})-ω	K	Ampl. (m)
Semidiurnal Species					
Principal Lunar	M_2	12.421h	$1.40519 \cdot 10^{-4}$	0.242334	
Principal Solar	S_2	12.000h	$1.45444 \cdot 10^{-4}$	0.112841	
Elliptical Lunar	N_2	12.658h	$1.37880 \cdot 10^{-4}$	0.046398	
Declination Luni-Solar	K_2	11.967h	$1.45842 \cdot 10^{-4}$	0.030704	
Diurnal Species					
Declination Luni-Solar	K_1	23.934h	$0.72921 \cdot 10^{-4}$	0.141565	
Principal lunar	O_1	25.819h	$0.67598 \cdot 10^{-4}$	0.100574	
Principal solar	P_1	24.066h	$0.72523 \cdot 10^{-4}$	0.046843	
Elliptical lunar	Q_1	26.868h	$0.64959 \cdot 10^{-4}$	0.019256	
Long-Period Species					
Fortnightly Lunar	Mf	13.661d	$0.053234 \cdot 10^{-4}$	0.041742	
Monthly Lunar	Mm	27.555d	$0.026392 \cdot 10^{-4}$	0.022026	
Semiannual Solar	Ssa	182.621d	$0.0038921 \cdot 10^{-4}$	0.019446	

2. ONE-DIMENSIONAL MOTION IN A CHANNEL.

Above equation we apply first for one-dimensional channel with the bathymetric cross-section corresponding to the typical depth distribution in the Gulf of Alaska (Fig. 1). The algorithm for the run-up in a channel is taken from Kowalik et. al., (2005).

At the right boundary a run-up algorithm was applied. At the left open boundary, a radiation condition based on the known tidal amplitude and current is prescribed (Flather, 1976; Durran, 1999; Kowalik, 2003).

The value of an invariant along incoming characteristic to the left boundary is defined as $(\zeta_p + u_p \sqrt{H/g})/2$ and for the smooth propagation into domain this value ought to be equal to the invariant specified inside computational domain in the close proximity to the boundary $(\zeta + u \sqrt{H/g})/2$. This yield equation for the velocity to be specified at the left boundary as

$$u = u_p - \sqrt{g/H}(\zeta - \zeta_p) \qquad (9)$$

In this formula ζ_p and u_p are prescribed tidal sea level and velocity. For one tidal constituent the sea level and velocity can be written as amplitude and phases of a periodical function:

$$\zeta_p = z_{amp}\cos(\omega t - z_{phase}) \quad \text{and} \quad u_p = u_{amp}\cos(\omega t - u_{phase}) \tag{10}$$

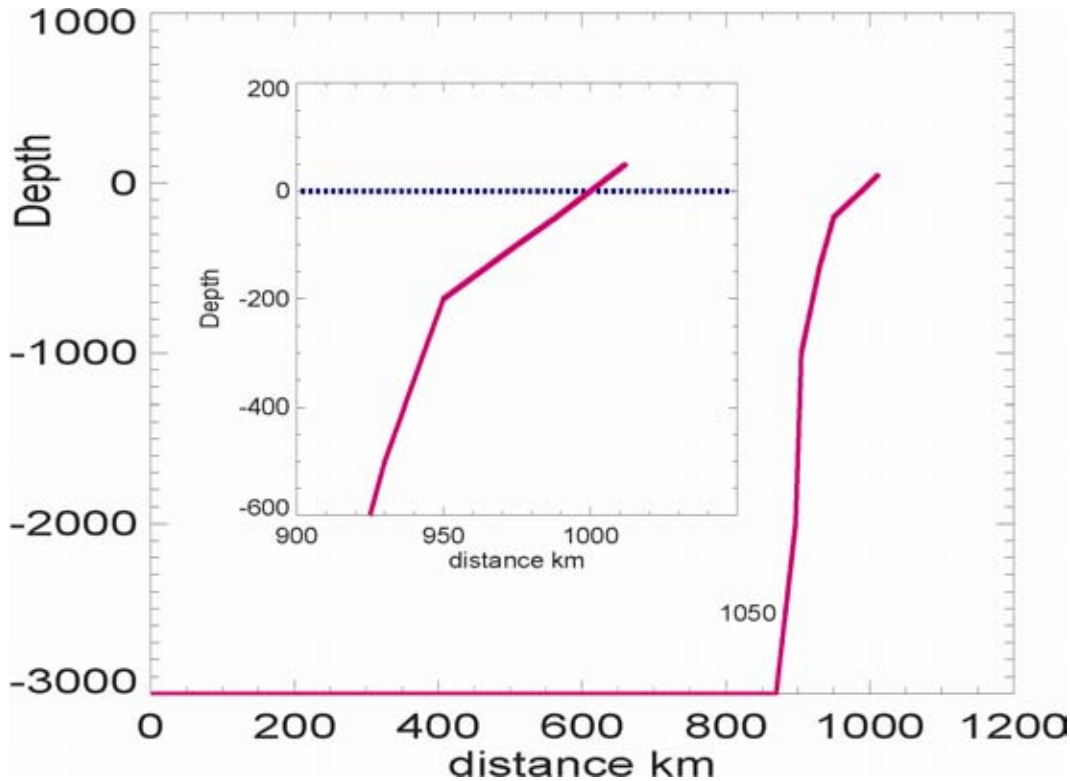Here ω is a frequency given in Table 1.

Figure 1. Typical bathymetry (in meters) profile cutting continental slope and shelf break in the Gulf of Alaska. Inset shows shelf and sloping beach.

We start computation by considering tsunami generated by an uniform bottom uplift at the region located between 200 and 400km of the 1-D canal from Fig. 1. Short-period tsunami waves require the high spatial and temporal resolution to reproduce runup and the processes taking place during the short time of tide and tsunami interaction. The space step is taken as 10m

As no tide is present in eq. (9) prescribed tidal sea level and velocity are set to zero.

In Figure 2, a 2m tsunami wave mirrors the uniform bottom uplift occurring at 40s from the beginning of the process Later, this water elevation splits into two waves of 1m height each traveling in opposite directions (T=16.7min). While the wave, traveling towards the open boundary, exits the domain without reflection (radiation condition), the wave, traveling towards the shelf, propagates without change of amplitude. This is because the bottom friction at 3km depth is negligible (T=39min). At T=57.6min, the tsunami impinges on the shelf break resulting in the tsunami splitting into two waves (T=1h16min) due to partial

reflection: a backward traveling wave with amplitude of ~0.5 m, and a forward traveling wave towards the very shallow domain (T=1h27min).

While the wave reflected from the shelf break travels without change of amplitude, the wave on the shelf is strongly amplified. The maximum amplitude attained is
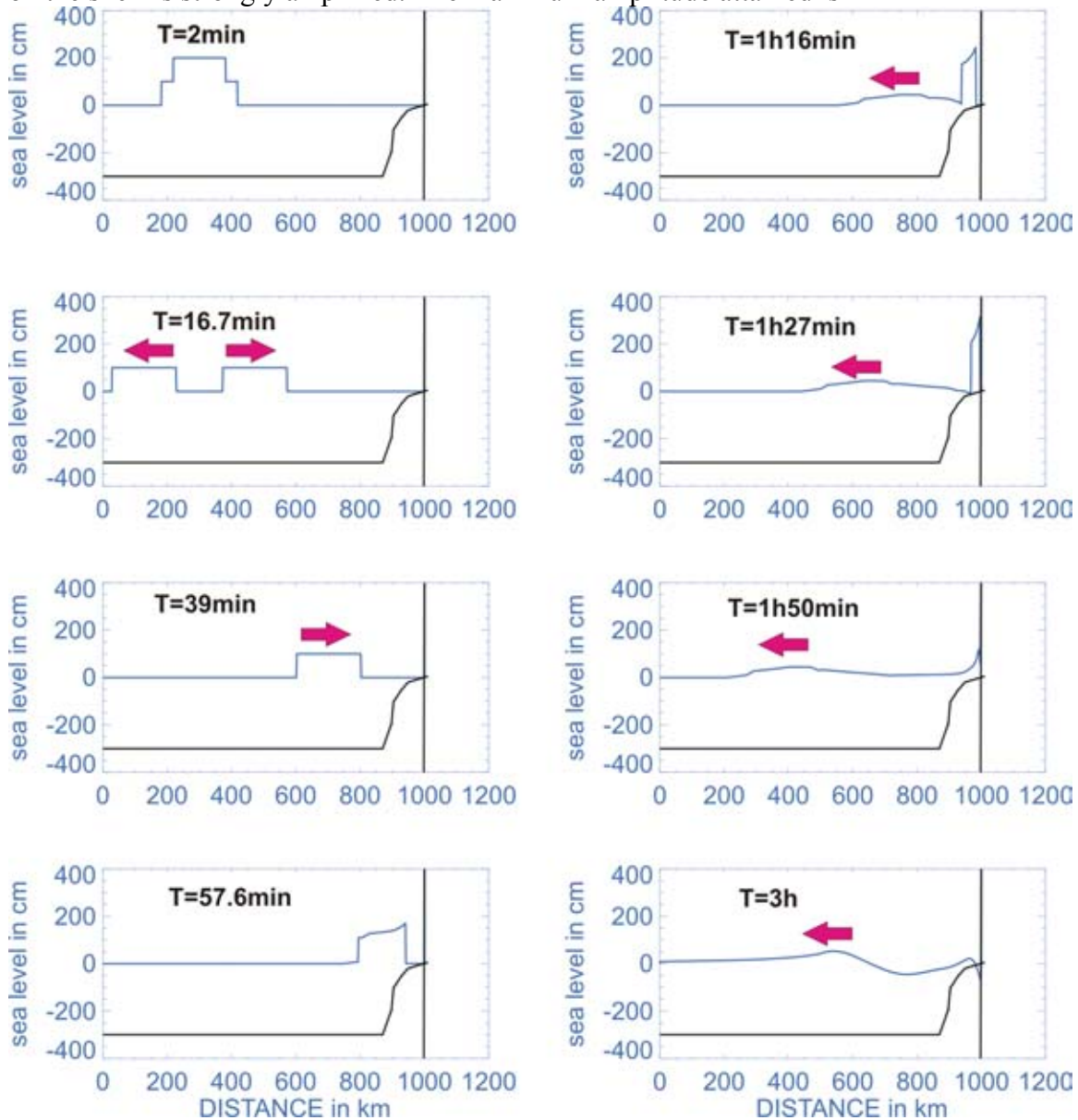
Figure 2. History of tsunami propagation. Generated by the bottom deformation at T=40s this tsunami wave experiences significant transformations and reflections. Black lines denote bathymetry. Vertical line denotes true bathymetry at the tsunami range from -4m to 4m. The second black lines repeats bathymetry from Figure 3, scale is 1:1000.

approximately 7.2m (not shown). Figure 2 (T=3h) shows the time when the wave reflected from the shelf break left the domain and the wave over the shelf oscillates with an amplitude

diminishing towards the open ocean. These trapped and partially leaky oscillations continue for many hours, slowly losing energy due to waves radiating into the open ocean and due to the bottom dissipation. This behavior is also described in Fig. 3, where temporal changes of the sea level and velocity are given at the two locations. At the boundary between dry and wet domain the sea level changes when runup reaches this location. It is interesting to note that repeated pulses of the positive sea level are associated with velocity which goes through the both positive and negative values. At the open boundary the initial box signal of about 20min period is followed by the wave reflected from the shelf break and the semi-periodic waves radiated back from the shelf/shelf break domain. The open boundary signal which is radiated into open ocean, is therefore superposition of the main wave and secondary waves. The period of the main wave is defined by the size of the bottom deformation and ocean depth (initial wave generated by earthquake) while the periods of the secondary waves are defined by reflection and generation of the new modes of oscillations through an interaction of the tsunami waves with the shelf/shelf break geometry.

In numerous publications (e.g. Munk, 1962; Clarke, 1974, Mei, 1989), it was shown that the shelf modes of oscillations usually dominate meteorological disturbances observed along coasts. The evidence for tsunamis trapped in a similar manner have been presented both, theoretically (Abe and Ishii, 1980) and in observations (Loomis, 1966; Yanuma and Tsuji, 1998; Mofjeld et. al., 1999).

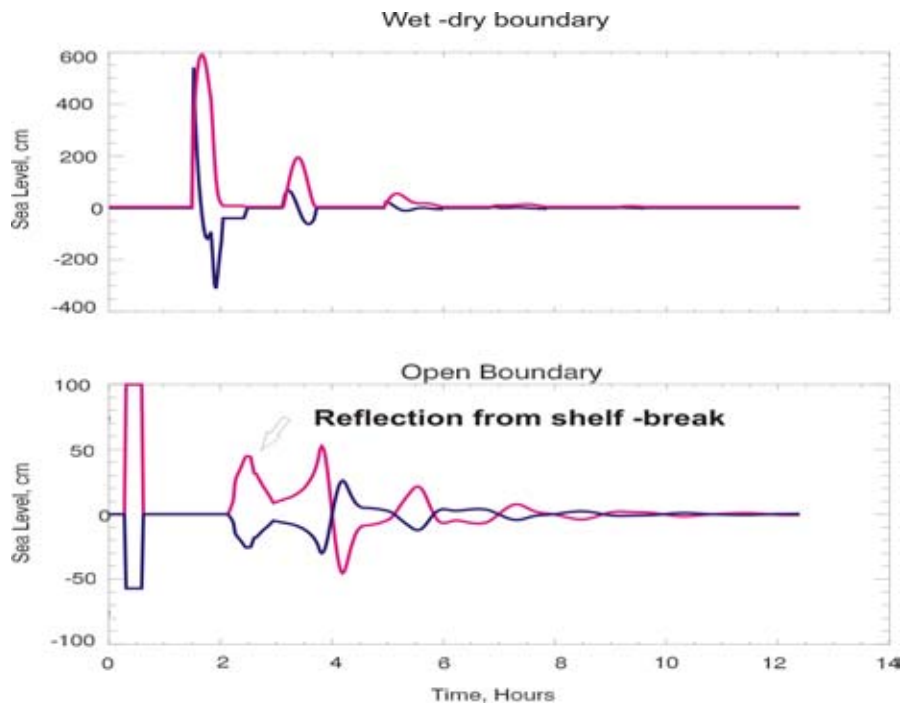Figure 3. Tsunami temporal change of the sea level (red) and velocity (blue) at the wet-dry boundary (upper panel) and at the open boundary (lower panel). Velocities are expressed in the cm/s, and the lower panel numbers should be divided by 10.

To investigated the tide wave behavior in the same channel we shall introduce into radiating boundary condition (eq. 9) the sea level and velocity in he form given by eq.(10),

$$\zeta_p = 273.19\cos(\omega t - 0.821484) \quad \text{and} \quad u_p = 16.6974\cos(\omega t - 5.53261) \tag{11}$$

Here omega is M_2 tide frequency (see Table 1). As boundary signal is transmitted into domain a stationary solution is obtained after five tidal periods. In Fig. 4 a three tidal period are given to depict tidal periodicity at the open and wet-dry boundaries. The entire solution included 10 periods.

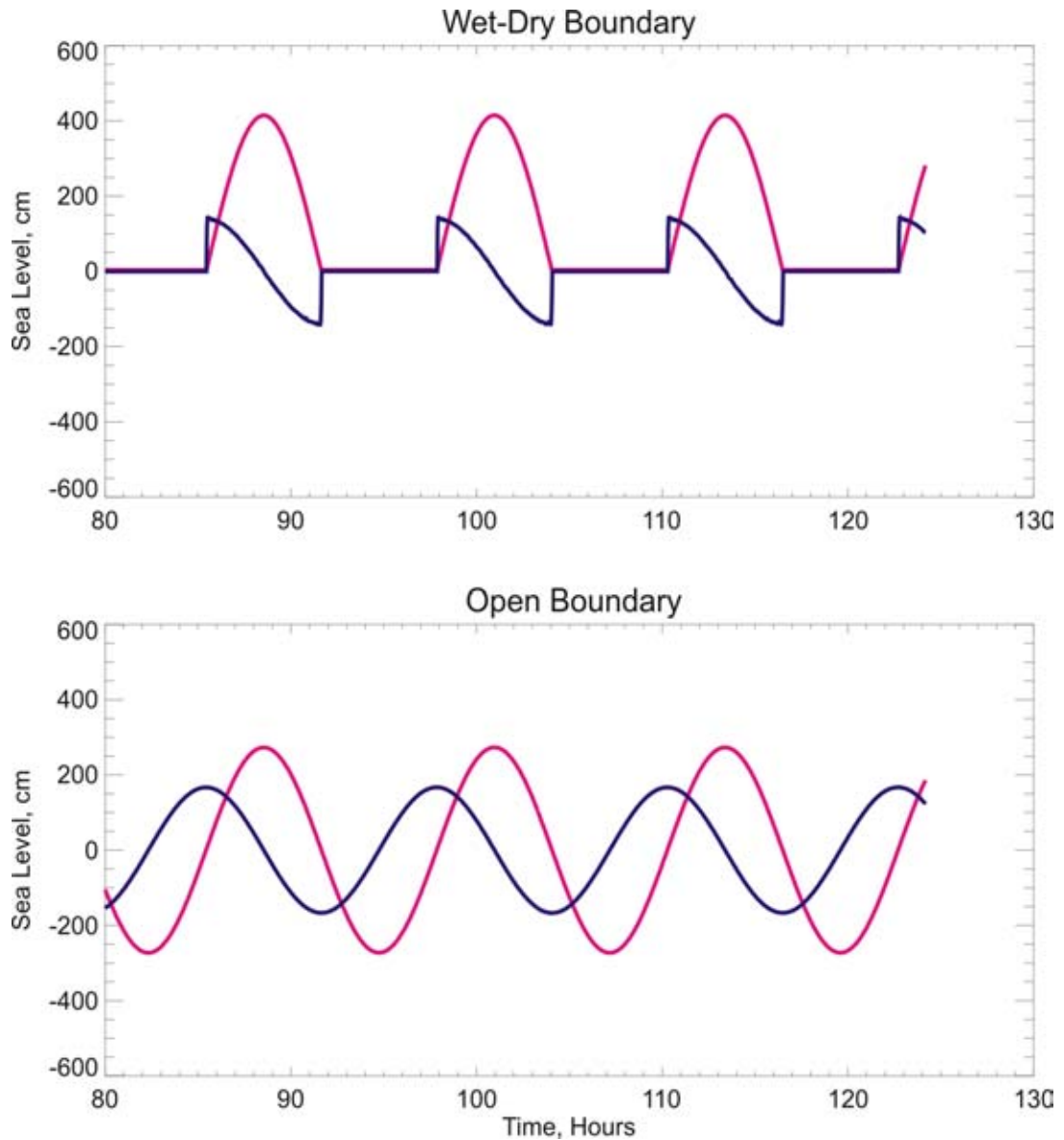Figure 4. M_2 tide temporal changes: sea level (red) and velocity (blue). Velocities are expressed in the cm/s, and in both panels numbers should be divided by 10.

As one shall expect the tidal signal is periodical in time and space with peculiarities in the region of the wet-dry boundary. The distribution of the tidal velocities and sea level along the channels shows that tide actually generated standing wave (Fig. 5), see Defant

(1960). In Fig. 5 the M_2 sea level and velocity is given along the channel for the four phases of the wave. These phases were chosen in proximity to the minimum, maximum and zero for the sea level and velocity.
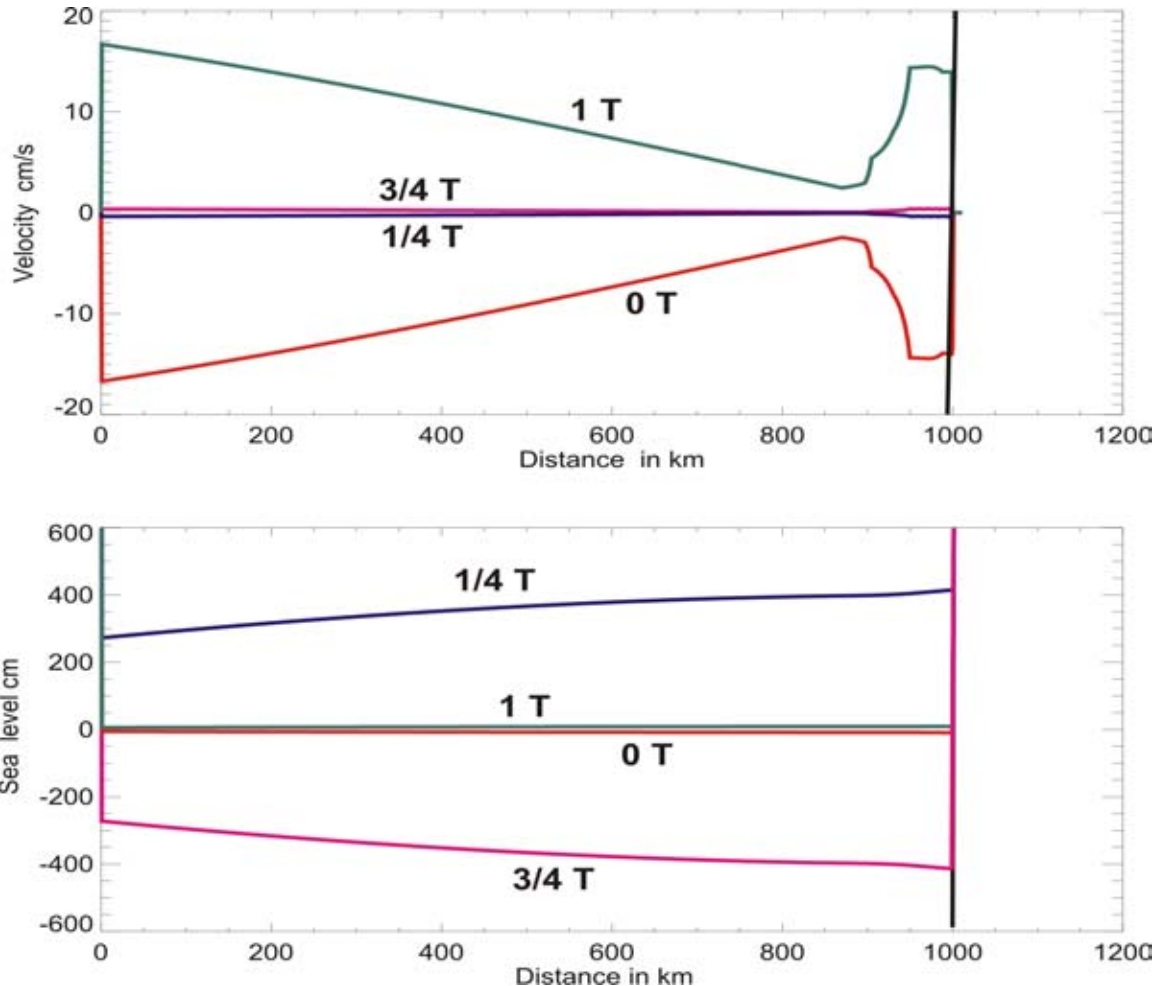
Figure 5. Velocity (upper panel) and sea level (lower panel) of the M2 tide along the channel at the four phases of 12.42 hour cycle.

The maximum or minimum of the sea level (and velocity) is having the same phase from the mouth to the head of the channel. The sea level show steady increase towards the channel's head, while the velocity is more differentiated with the minimum in proximity to the shelf break. The slow change of tidal parameters along the channel is juxtaposed against the faster change of the tsunami parameters with 20min variability generated by the bottom deformation (Fig. 3, lower panel). The resulting tide-tsunami interactions are described in Fig. 6. The tsunami is generated in such a fashion that it will arrive to the shore when the tidal amplitude achieve maximum. The joint amplitude of tide and in proximity to the wet-

dry boundary is close to 10m (Fig. 6 upper panel). The signal radiated from the domain is given in Fig.6, lower panel. This signal when detided depicts the same tsunami as in Fig. 3 (lower panel).   We may conclude that the tides and tsunami propagating in channel from Fig. 1 are superposed in a linear fashion. This is due mainly to the small tidal currents.

Wet-Dry Boundary
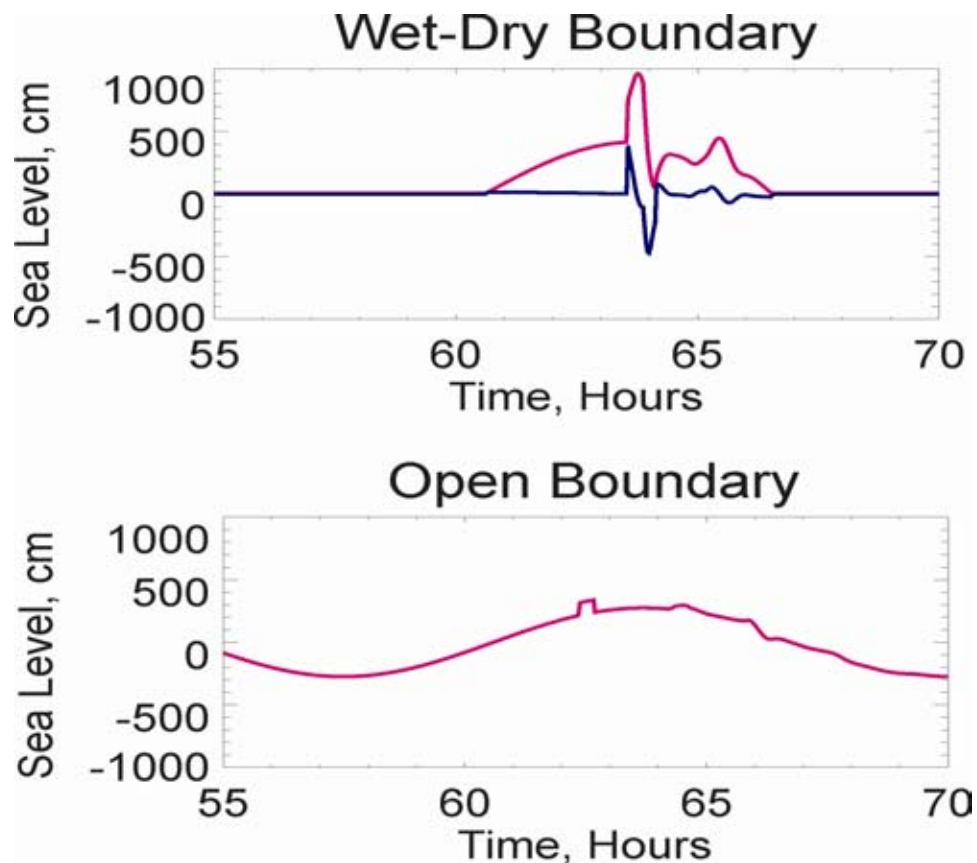
Open Boundary

Figure 6. Tsunami and tide temporal change of the sea level (red) and velocity (blue) at the wet-dry boundary (upper panel) and at the open boundary (lower panel).

To elucidate tide/tsunami interaction in the wet-dry region, we superpose the maximum of sea levels and velocities along the channel obtained through the independent computation of tides and tsunami, and tsunami and tides computed as one process given in Fig.6. The last 20km before the wet-dry boundary are shown in Fig. 7. While tide (green color) show very small amplitude increase (upper panel, maximum 415cm) and very small velocity (lower panel, maximum is 16.7cm/s), the tsunami (blue color) is strongly enhanced in both sea level (maximum 721cm) and velocity (maximum 627cm/s). The dry domain starts

at the 1000km and the horizontal runup due to the tide is 980 m and due to the tsunami is 1700m. By adding together the results from the two independent computations (red line) we are able to obtain the distribution of maximum of the sea level and velocity but not a joint runup. Joint computation moves the sea level and velocity into previously dry domain (dashed lines). As in the previous experiment the tidal velocity was relatively very small a nonlinear interaction could occur only for the short time span in the very shallow water where sea level change due to tide and tsunami is of the order of depth.
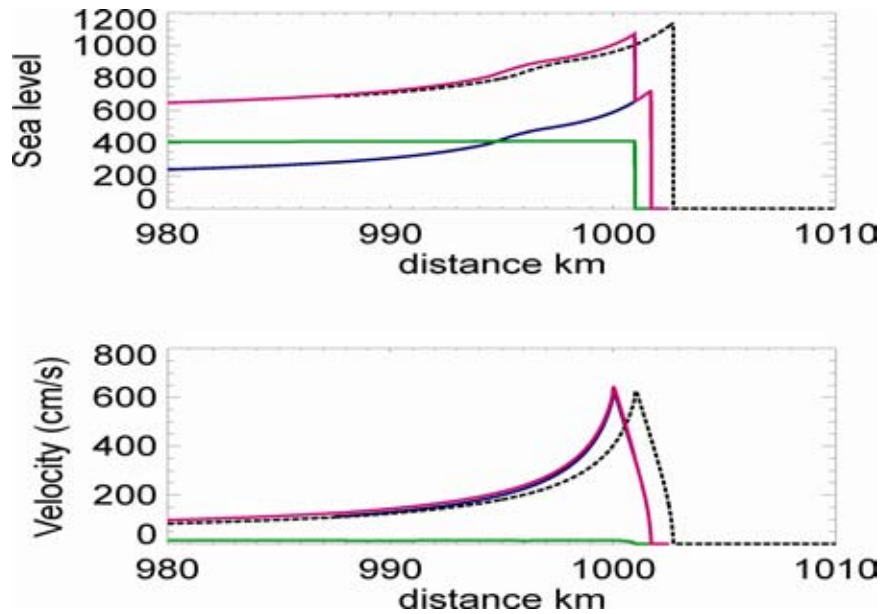
Figure 7. Distribution of the maximum of velocity (lower panel) and sea level (upper panel). Green lines: only tides; blue lines: only tsunami; red lines: superposition of tides and tsunami; dashed lines: joint computation of tides and tsunami.
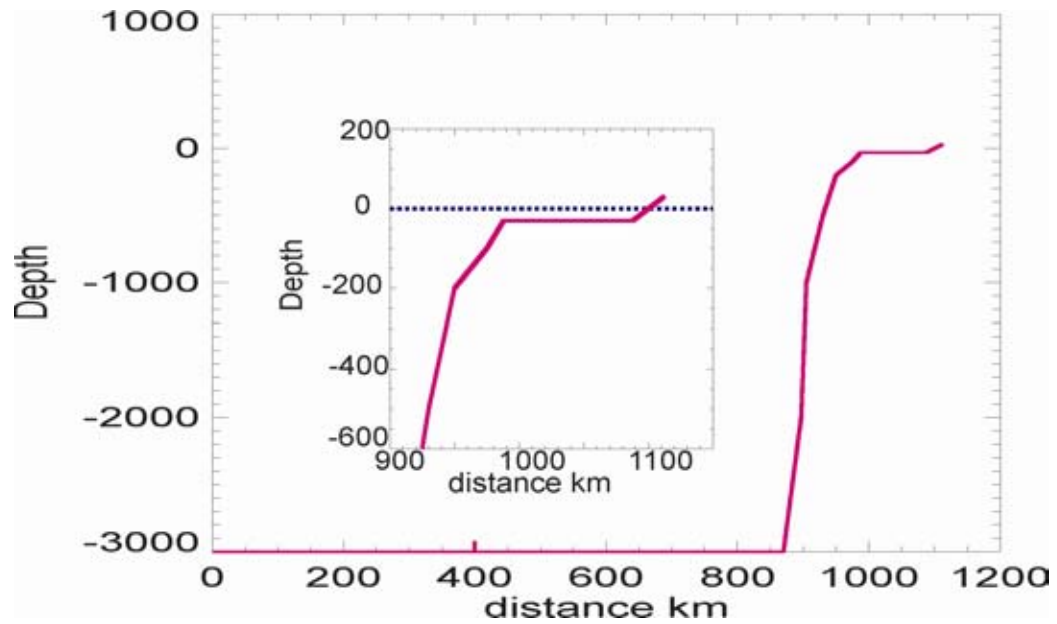
Figure 8. Typical bathymetry profile cutting continental slope and shelf break in the Gulf of Alaska. To imitate shallow water bodies connected to the Gulf a 100km of 30m depth (insert) is added to the profile from Fig. 1.

We consider now a similar depth distribution to the Fig. 1 but to enlarge tidal velocity a shallow channel of the 100km long is introduced between 990km and 1090km (see Fig. 8). This channel imitates the water bodies like Cook Inlet with extended shallow depth and strong transformation of the current.

Figure 9. Distribution along the channel of the maximum of tsunami velocity (blue lines)) and tsunami sea level (red lines). Upper panel: along the entire channel. Lower panels: along the shelf.

The results for the computed tsunami are given as distributions of maximum sea level and velocity along the channel (Fig. 9). In tsunami approaching shallow water channel both sea level and velocity are amplified, but this amplification is slowly dissipated along 100km channel due to the bottom friction. Again both velocity and sea level are strongly enhanced on the sloping beach. Maximum current in the sloping beach region is 487cm/s and the sea level increases to 495cm. Thus comparing with the previously considered propagation which resulted in 721cm of the maximum sea level, the strong reduction of the sea level is observed and can be attributed to the shallow water dissipation.

The behavior of the M_2 tide is described in the Figure 10.

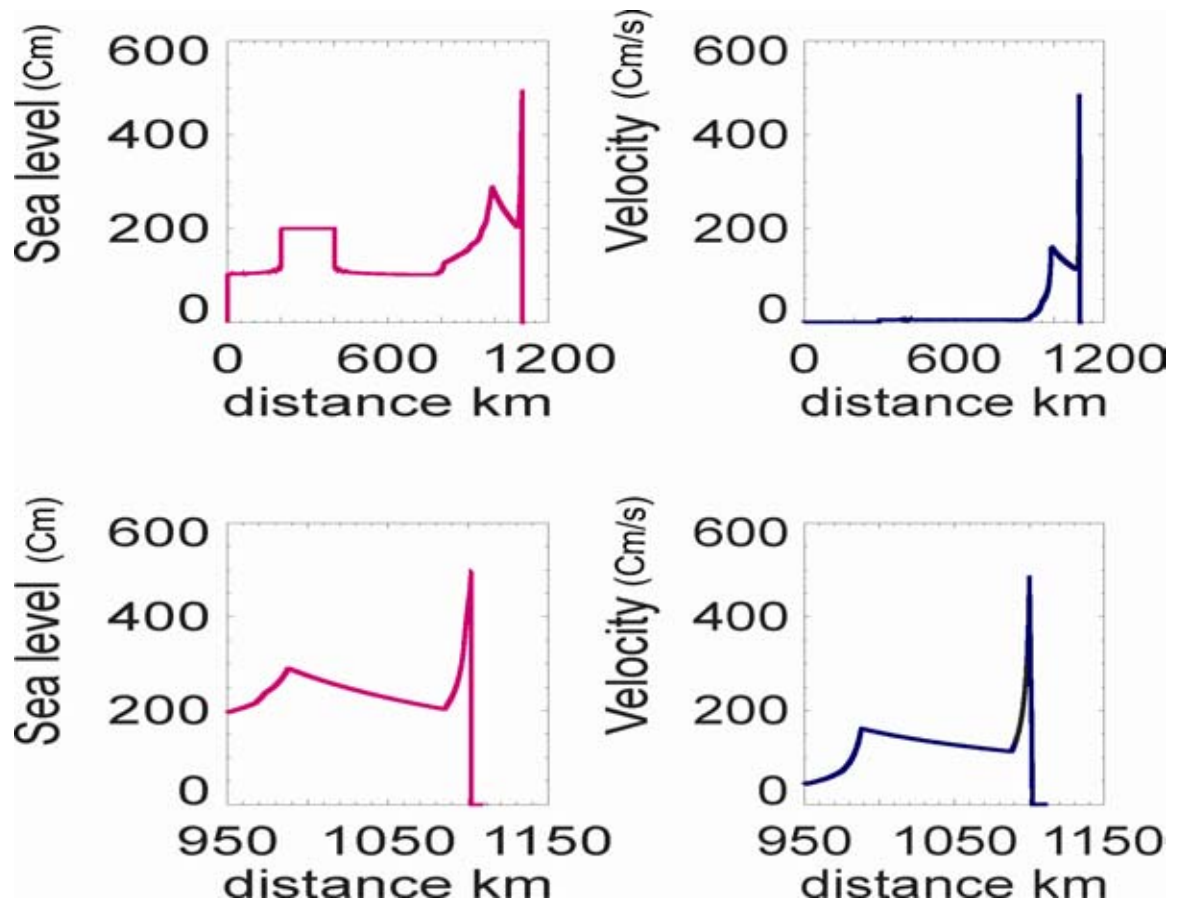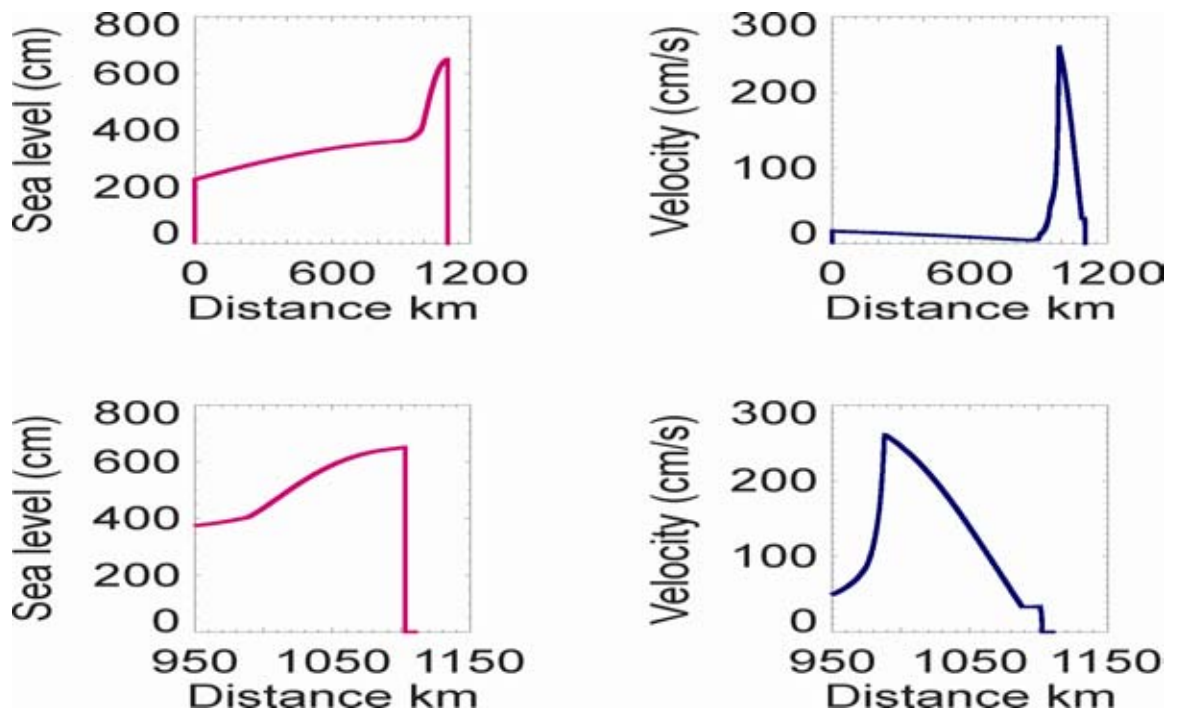Figure 10. Distribution along the channel of the maximum of tide velocity (blue lines)) and tide sea level (red lines). Upper panel: along the entire channel. Lower panels: along the shelf.

The tide dynamics along the channel is quite different from the tsunami. Upon entering from the deep ocean into shallow channel both tide and tsunami sea level is amplified. Along the 100km channel the sea level of the tsunami steady diminishes while the tide sea level is steady increasing. On the other hand both tsunami and tide currents are dissipated along the channel. But the most conspicuous difference occurs in the sloping beach portion of the channel. Whereas along the short distance of 10km the tsunami current and sea level is amplified about 2-3 times, the tidal sea level is showing a few cm increase and tidal current is constant along this shallow water. The relatively large tidal (apr. 260cm/s) and tsunami (apr. 160cm/s) velocity in the shallow channel may reasonably be assumed as the primary source of the nonlinear interactions between tide and tsunami.

 In the joint tsunami/tide signal (Fig. 11) two regions of enhanced currents have been generated; one at the entrance to the shallow water channel where tidal current dominates and the second at the beach where tsunami current dominates. The nonlinear interactions have been elucidated in Fig. 11. While superposed signal of tide and tsunami (red lines) and jointly computed tide and tsunami (dash black lines) are the same in the deep water channel, they diverge in the shallow water channel. Both sea level and velocity in the joint computation have smaller values than the signal obtained by superposition. We may conclude that the joint signal has been reduced due to tide/tsunami nonlinear interaction.
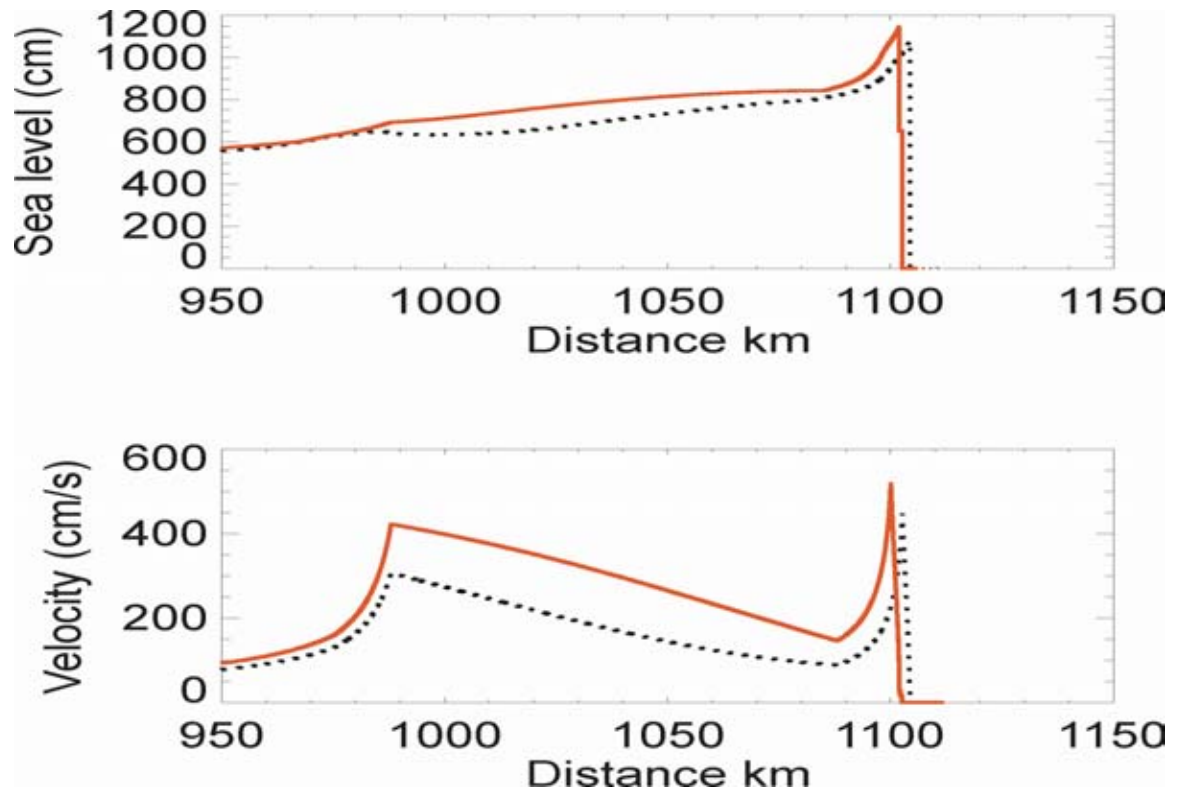
Figure 11. Distribution of the maximum of velocity (lower panel) and sea level (upper panel) in the shallow part of the channel. Red lines: linear superposition of tides and tsunami simulated separately; dashed lines:show results for tides and tsunami simulated together and resulted in their non-linear interaction.

3. DISCUSSION AND CONCLUSION.

Two simple cases of tide/tsunami interactions along the narrow and wide shelf have been investigated to define importance the nonlinear interactions. In a channel with narrow shelf the time for the tide/tsunami interactions is very short and mainly limited to the large currents in the runup domain. In the channel with extended shallow water region the nonlinear bottom dissipation of the tide and tsunami leads to strong reduction in tsunami amplitude and tsunami currents. The tidal currents and amplitude remain unchanged through interaction with tsunami. The main difference in behavior of tide and tsunami is related to the wave length, while M_2 tide in the 3km deep ocean has wavelength of 7670km, the wavelength of 20min period tsunami is only 206km. The 100km shallow water channel is a half-wavelength for tsunami but only 1.3% of the tide wavelength. The major difference between tide and tsunami occurs in the runup region. Tide does not undergo changes in the velocity or sea level in the nearshore/runup domain while for tsunami this is the region of major amplification of the seal level and currents.

In summary, the energy of an incident tsunami can be redistributed in time and space with the characteristics which differ from the original (incident) wave. These changes are induced by the nonlinear shallow water dynamics and by the trapped and partially leaky oscillations controlled by the continental slope/shelf topography. The amplification of

tsunami amplitude is mainly associated with strong amplification of tsunami currents. The nonlinear interaction of the tide with tsunami is important, as it generates stronger sea level change and even stronger changes in tsunami currents, thus the resulting run-up ought to be calculated for the tsunami and tide propagating together.

REFERENCES:

Abe, K. and Ishii, H. 1980. Propagation of tsunami on a linear slope between two flat regions. Part II reflection and transmission, J. Phys. Earth, 28, 543-552.

Clarke, D. J. 1974. Long edge waves over a continental shelf, Deutsche Hydr. Zeit., 27, 1, 1-8.

Defant, A., 1960. Physical Oceanography, Pergamon Press, v 2, 598pp.

Durran, D. R. 1999. Numerical Methods for Wave Equations in Geophysical Fluid Dynamics, Springer, 465pp.

Flather, R.A. 1976. A tidal model of the north-west European continental shelf. Mem. Soc. R. Sci. Lege, 6, 141-164.

Kowalik, Z. 2003. Basic Relations Between Tsunami Calculation and Their Physics - II, Science of Tsunami Hazards, v. 21, No. 3, 154-173

Kowalik Z., W. Knight, T. Logan, and P. Whitmore. 2005a. NUMERICAL MODELING OF THE GLOBAL TSUNAMI: Indonesian Tsunami of 26 December 2004. Science of Tsunami Hazards, Vol. 23, No. 1, 40- 56.

Kowalik, Z., and A. Yu. Proshutinsky, 1994. The Arctic Ocean Tides, In: The Polar Oceans and Their Role in Shaping the Global Environment: Nansen Centennial Volume, Geoph. Monograph 85, AGU, 137--158.

Loomis, H. G. 1966. Spectral analysis of tsunami records from stations in the Hawaiian Islands. Bull. Seis. Soc. Amer. 56, 3 697-713.

Mei, C. C. 1989. The Applied Dynamics of Ocean Surface Waves, World Scientific, 740 pp.

Mofjeld, H.O., V.V. Titov, F.I. Gonzalez, and J.C. Newman (1999): Tsunami wave scattering in the North Pacific. IUGG 99 Abstracts, Week B, July 26–30, 1999, B.132.

Munk, W. H. 1962. Long ocean waves, In: The Sea, v. 1, Ed. M. N. Hill, InterScience Publ., 647-663.

Weisz, R. and C. Winter. 2005. Tsunami, tides and run-up: a numerical study, Proceedings of the International Tsunami Symposium, Eds.: G.A. Papadopoulos and K. Satake, Chania, Greece, 27-29 June, 2005, 322.

Pugh, D. T.. 1987. Tides, Surges and Mean Sea-Level, John Wiley & Sons, 472pp.

Yanuma, T. and Tsuji Y. 1998. Observation of Edge Waves Trapped on the Continental Shelf in the Vicinity of Makurazaki Harbor, Kyushu, Japan. Journal of Oceanography, 54, 9 -18.

CONFIRMATION AND CALIBRATION OF COMPUTER MODELING OF TSUNAMIS PRODUCED BY AUGUSTINE VOLCANO, ALASKA

James E. Beget
Geophysical Institute and Alaska Volcano Observatory
University of Alaska, Fairbanks, AK, USA

Zygmunt Kowalik
Institute of Marine Sciences
University of Alaska, Fairbanks, AK, USA

ABSTRACT

Numerical modeling has been used to calculate the characteristics of a tsunami generated by a landslide into Cook Inlet from Augustine Volcano. The modeling predicts travel times of ca. 50-75 minutes to the nearest populated areas, and indicates that significant wave amplification occurs near Mt. Iliamna on the western side of Cook Inlet, and near the Nanwelak and the Homer-Anchor Point areas on the east side of Cook Inlet. Augustine volcano last produced a tsunami during an eruption in 1883, and field evidence of the extent and height of the 1883 tsunamis can be used to test and constrain the results of the computer modeling. Tsunami deposits on Augustine Island indicate waves near the landslide source were more than 19 m high, while 1883 tsunami deposits in distal sites record waves 6-8 m high. Paleotsunami deposits were found at sites along the coast near Mt. Iliamna, Nanwelak, and Homer, consistent with numerical modeling indicating significant tsunami wave amplification occurs in these areas.

1. INTRODUCTION

Augustine Volcano is the most active volcano in the Cook Inlet region of Alaska (Fig. 1). It erupted at least five times during the 20th century, and began erupting again in December 2005. The activity in early 2006 has included multiple episodes of explosive ash and pyroclastic flow eruptions, as well as lava dome eruptions at the summit of the volcano.   The steep summit edifice of Augustine Volcano repeatedly collapsed in giant debris avalanches into the sea around Augustine Island during the last 2000 years, most recently in 1883 (Beget and Kienle, 1992; Siebert et al., 1995). Volcanic debris avalanches into the sea are an important cause of tsunamis (Beget, 2000).
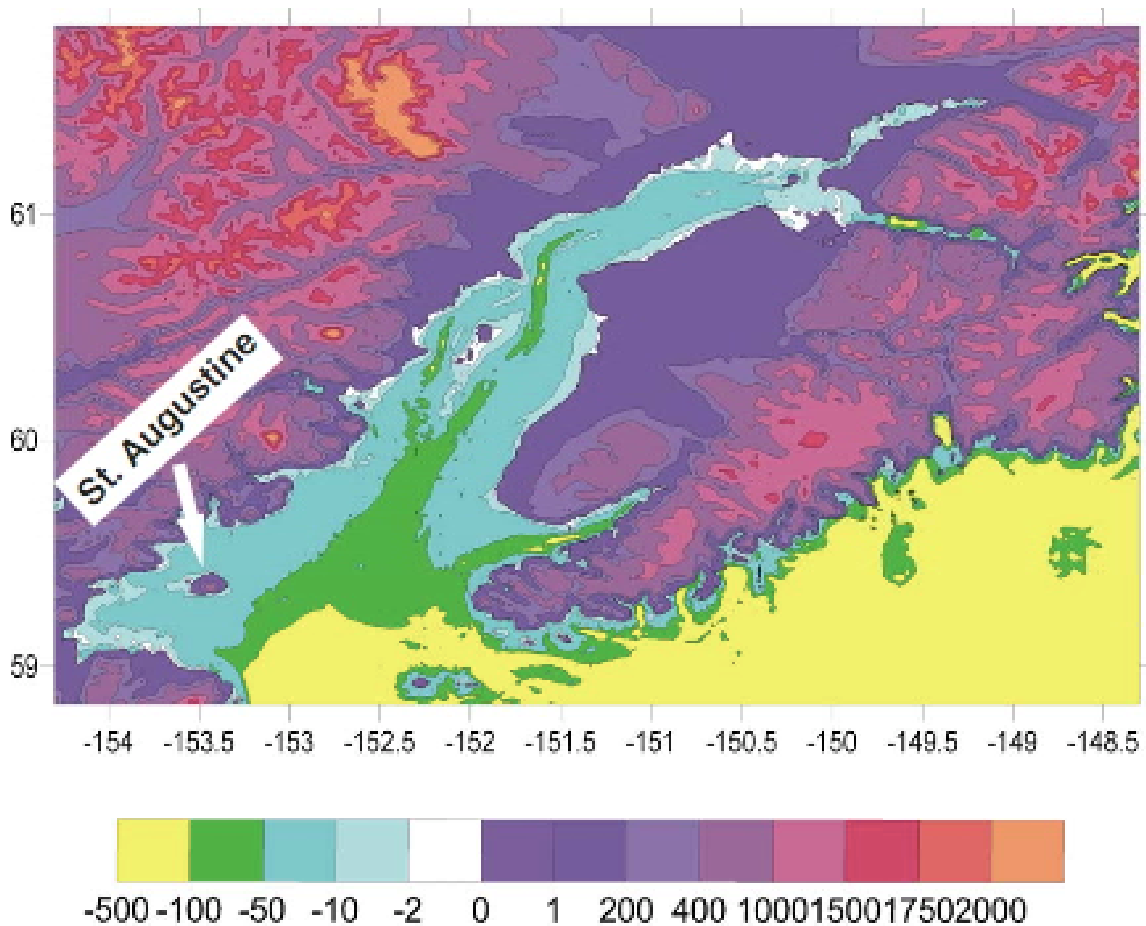

Fig. 1. Location of Augustine Volcano within Cook Inlet, Alaska, and generalized bathymetry of Cook Inlet.

On the morning of October 6, 1883, a debris avalanche from the north flank of Augustine Volcano travelled northward from the summit of the volcano to the shoreline of Augustine Island and then flowed 5 km into the waters of Cook Inlet, generating a tsunami (Kienle et al., 1987; Siebert et al., 1989).   A contemporary written account of the tsunami recorded in a log at a trading post at English Bay (modern Nanwalek), about 80 km northeast of the volcano, states (Alaska Commercial Company, 1883):

"At this morning at 8:15 o'clock, 4 tidal waves flowed with a
Westerly current, one following the other at the rate of 30 miles p.
Hour into the shore, the sea rising 20 feet above the usual level.
At the same time the air became black and fogy, and it began to
Thunder. With this at the same time it began to rain a finely
Powdered Brimstone Ashes, which lasted for about 10 minutes, and
Which covered everything to a depth of over 1/4 inch…the rain of
Ashes commencing again at 11 o'clock and lasting all day."

Cook Inlet has one of the largest tidal ranges on earth, and the 1883 Augustine tsunami occurred just at low tide. The 20 foot (ca. 6.6 m) waves at English Bay were just slightly larger than the tidal range in this area, mitigating the effects of the tsunami wave on coastal communities.   There were no reported fatalities from the 1883 tsunami, but oral history accounts, collected from Alaskan native people affected by the tsunami, tell of flooded coastal dwellings and kayaks washed away by the tsunami.

2. NUMERICAL MODEL OF TSUNAMI GENERATED FROM AUGUSTINE VOLCANO

The numerical model assumes that a portion of Augustine volcano collapsed into the shallow water of Cook Inlet, and is used to calculate a tsunami generated by the landslide from the volcano collapse. The source of debris is assumed to be the northeast side of the volcano's summit.

The model is based on geologically reasonable parameters derived from the extent and characteristics of past debris avalanches at Augustine Volcano determined through stratigraphic studies of the volcanic deposits and geologic mapping of Augustine Island (Waitt and Beget, 1996; Beget and Kienle, 1992). As the slide travelled into Cook Inlet, it's velocity is assumed to diminish from 50m/s to 10m/s, its thickness along the center of the slide also diminished from 30m to 10m, and the slide width increased from approximately 2.5km to 3.5km (fig. 2). The debris avalanche was simulated as progressive flow of the bottom uplift which imparted motion to the water column.
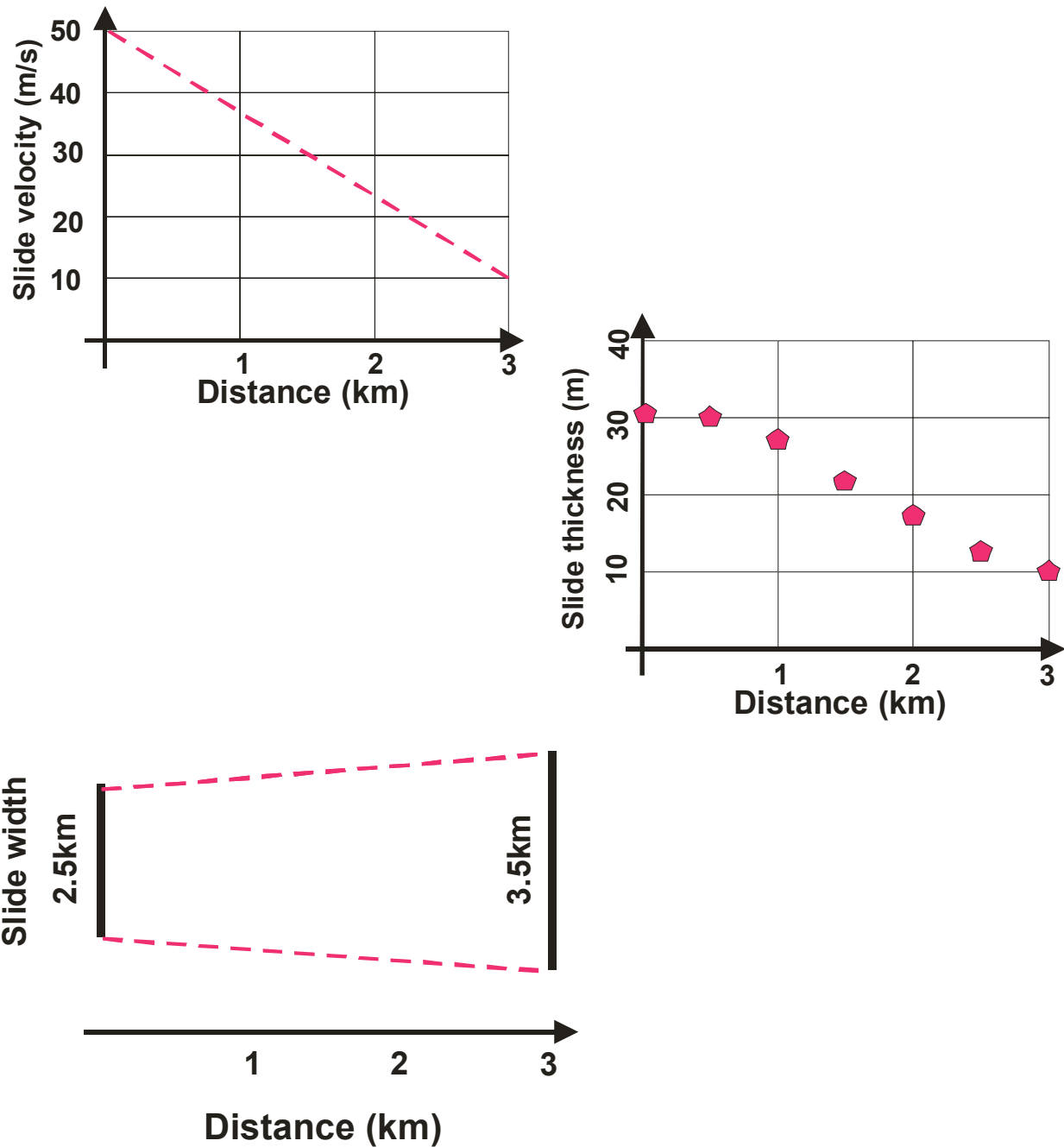
Figure 2. Slide velocity, thickness and width as a function of the distance for an eastern Augustine Volcano slide.

Generation and propagation of the tsunami is calculated by using a set of equations of motion and continuity for the long wave equations. Numerical form of these equations and appropriate boundary conditions for the land/water and water/water boundaries have been described by Kowalik et al. (2005). The finite-difference equations are solved in the spherical system of coordinate with the grid spacing of 1 minute along E-W

direction and 0.5 minute along N-S direction. The Cook Inlet domain depicted in Figure 2 span from 58 50'N to 6150'N and from 154 18'W to 148 18'W. A generalized map of the bathymetry of Cook Inlet is shown in figure one.

The first result of the numerical computation are travel times to various locations around lower Cook Inlet (Fig. 3). Tsunami travel time to Homer, the closest major population center to Augustine Volcano, is close to 75min, while travel time to Anchorage is around 4 hours.
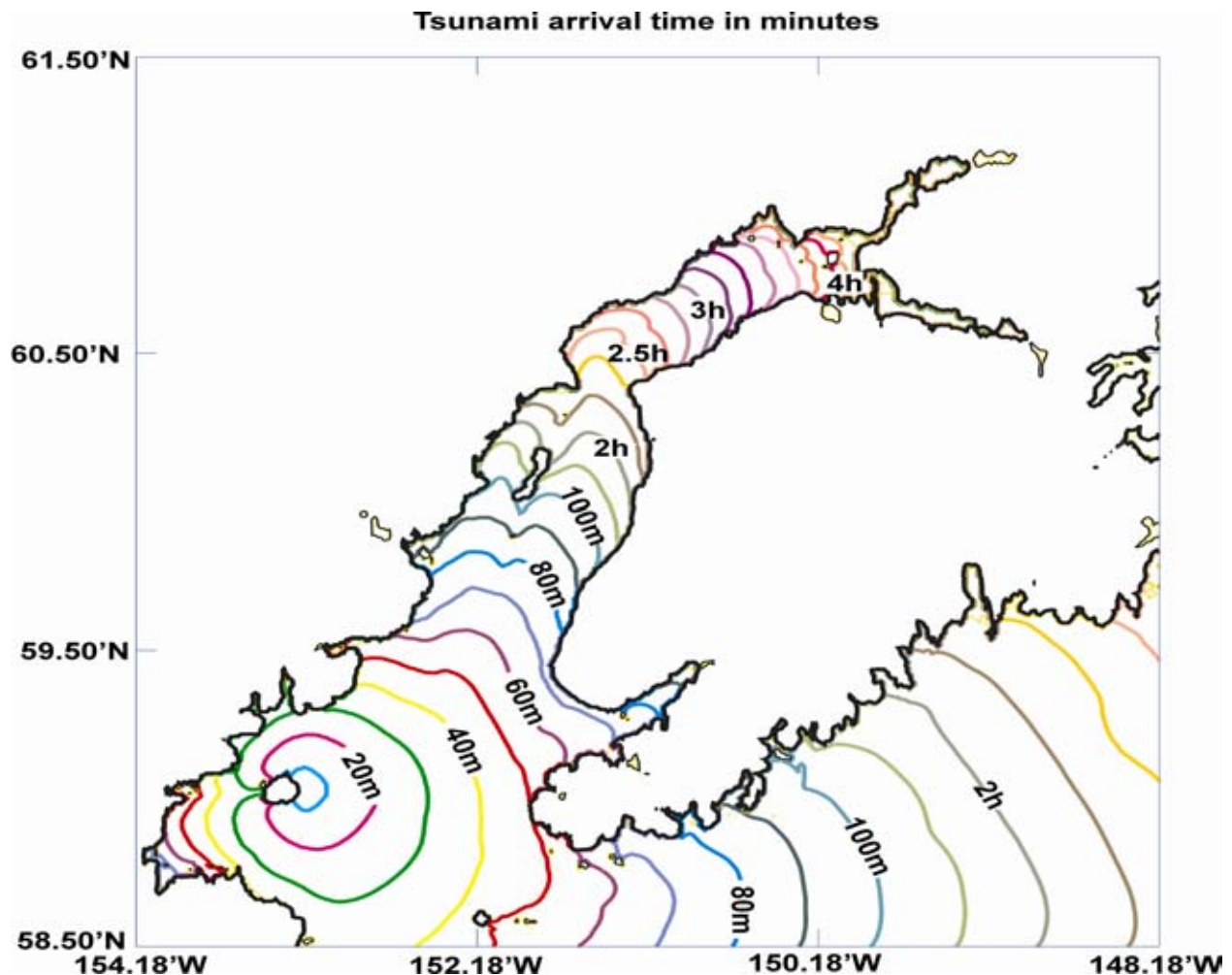
Figure 3. Tsunami arrival time estimated for the modeled slide from Augustine Volcano.

Another result of the numerical model are estimates of maximum tsunami amplitude, i.e. the maximum wave height which occurs during the 5 hours span after the landslide (fig. 4). In general, wave height maximums at the different grid points occur at different time. The spatial distribution of the maximum amplitude defines directional properties of the tsunami source, and therefore the maximum in Figure 4 is initially directed away from St. Augustine towards the east. While propagating towards shorelines the tsunami amplitude is amplified along peninsulas and along ridges. Towards the west from Augustine Island tsunami amplitude is reduced through bottom friction in the shallow waters of Kamishak Bay. The strongest amplification occurs

along the Seldovia-English Bay shoreline, up to approximately 2.5 m above the mean sea level (Fig. 4). Amplification of up to 2 m takes place along Anchor Point-Homer shoreline and along the Iliamna Volcano shoreline on the west side of Cook Inlet. This amplification is especially important for the coastal communities along the eastern shore of Lower Cook Inlet as tsunami travels to the Seldovia and English Bay areas in 50 min and to the Anchor Point and Homer areas in about 75 min, so that warning time for these communities is quite short.

TSUNAMI MAXIMUM AMPLITUDE

Figure 4. Maximum tsunami amplitudes in centimeters. Abbreviations: APH, Anchor Point –Homer; SEB Seldovia-English Bay; ILV, Iliamna Volcano.

3. COMPARISON OF NUMERICAL MODELING AND GEOLOGIC FIELD DATA
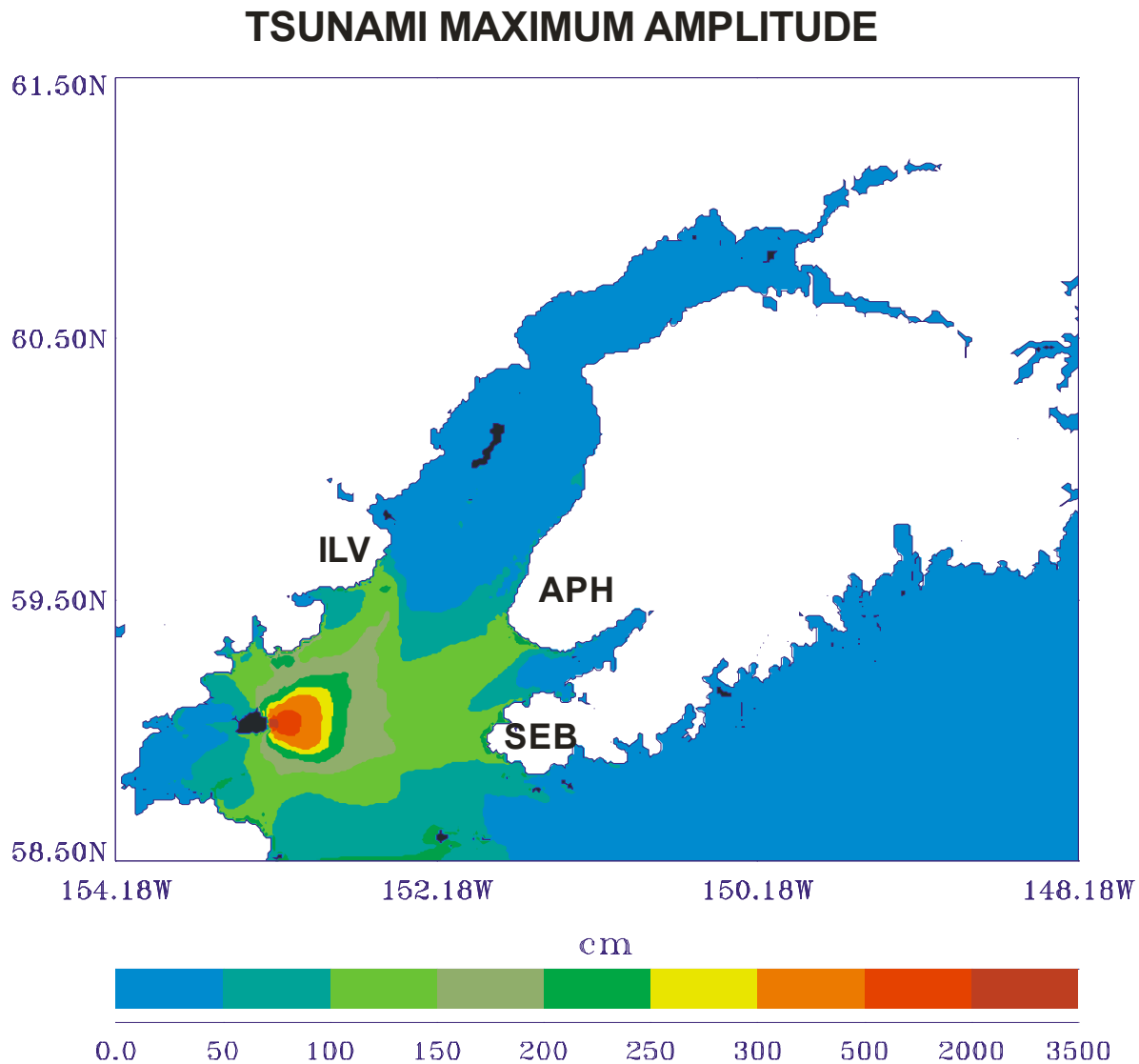
The 1883 avalanche from Augustine Volcano buried the former shoreline of Augustine Island, and displaced the new shoreline 2 km seaward at Burr Point. Bathymetry indicates the 1883 debris avalanche traveled an additional 3 kilometers farther northward beneath the sea (Waitt and Beget, 1996; Beget and Kienle, 1992). The horseshoe shaped crater left by the 1883 sector collapse had a volume of ca. 0.5 km3, and is probably a good approximation of the the volume of the debris avalanche itself.

In several locations near the current coastline paleotsunami deposits ranging from 10-230 cm in thickness and consisting mainly of mud and mollusc shells, but also including packages of beach sand and rounded pumice occur on top of hummocks of the 1883 debris avalanche at elevations ranging from 12-15 m above the high tide line. The presence of rounded pumice and incorporated marine fossils are similar to the sedimentological characteristics of tsunami deposits from the Krakatoa eruption (Carey et al., 2000). The 1883 Augustine tsunami deposits are overlain by 1883 tephra from Augustine volcano and by1912 Katmai tephra, confirming that they record the 1883 tsunami. Because the tsunami occurred at low tide, the original wave height near the source at Augustine Island must have been greater than 20 m. This agrees well with the numerical modeling of the proximal tsunami wave (fig. 4).

Distal 1883 tsunami deposits have been difficult to locate, because the wave height is similar to the ca. 8 m tidal range and the tsunami occurred at low tide. However, recent work has identified paleotsunami deposits at several localities around Cook Inlet. At English Bay (now called Nanwelak) the 1883 tsunami deposits occur at elevations virtually identical to the wave heights reported in the eyewitness account from this area. These deposits can be dated because the 1883 volcanic ash from Augustine Volcano directly overlies the layer of marine sands and cobbles found in low-lying coastal area, which in turn is overlain by the 1912 Katmai tephra (fig. 5).

Distal 1883 tsunami deposits are also found near Cannery Creek, along the Iliamna Volcano shoreline, where they occur more than a m above the high tide line (Anders and Beget, 1999). Other distal 1883 tsunami deposits are found in cores from tidal lagoons near Homer. The localities where the 1883 deposits have been found correspond with sites where numerical modeling shows that wave amplification occurs.

Waythomas (2000) discounted historic accounts of the 1883 Augustine tsunami after finding no paleotsunami deposits during a regional survey. However, the local amplification of tsunamis indicated by the numerical modeling suggests that the major impacts of some Augustine tsunamis may occur only in restricted areas of higher runup.

The tsunami generated by the 1964 Good Friday 9.2 M earthquake in Alaska affected much of lower Cook Inlet, and provides an interesting comparison to the 1883 Augustine event, as the 1964 tsunami was also about 6 m high in the lower Cook Inlet area, similar to the reported height of the Augustine tsunami, and also occurred near low tide. The 1964 tsunami caused significant damage to waterfront docks and buildings in Seldovia. Local residents in Seldovia and English Bay who had lived there

during the 1964 tsunami can point out the high water lines they observed. Paleotsunami deposits of sand, rounded beach gravel and drift wood from the 1964 event occur in these areas. The sedimentology of the 1964 tsunami deposits in the English Bay and Seldovia areas are identical to those of the 1883 tsunami deposits we report on here.
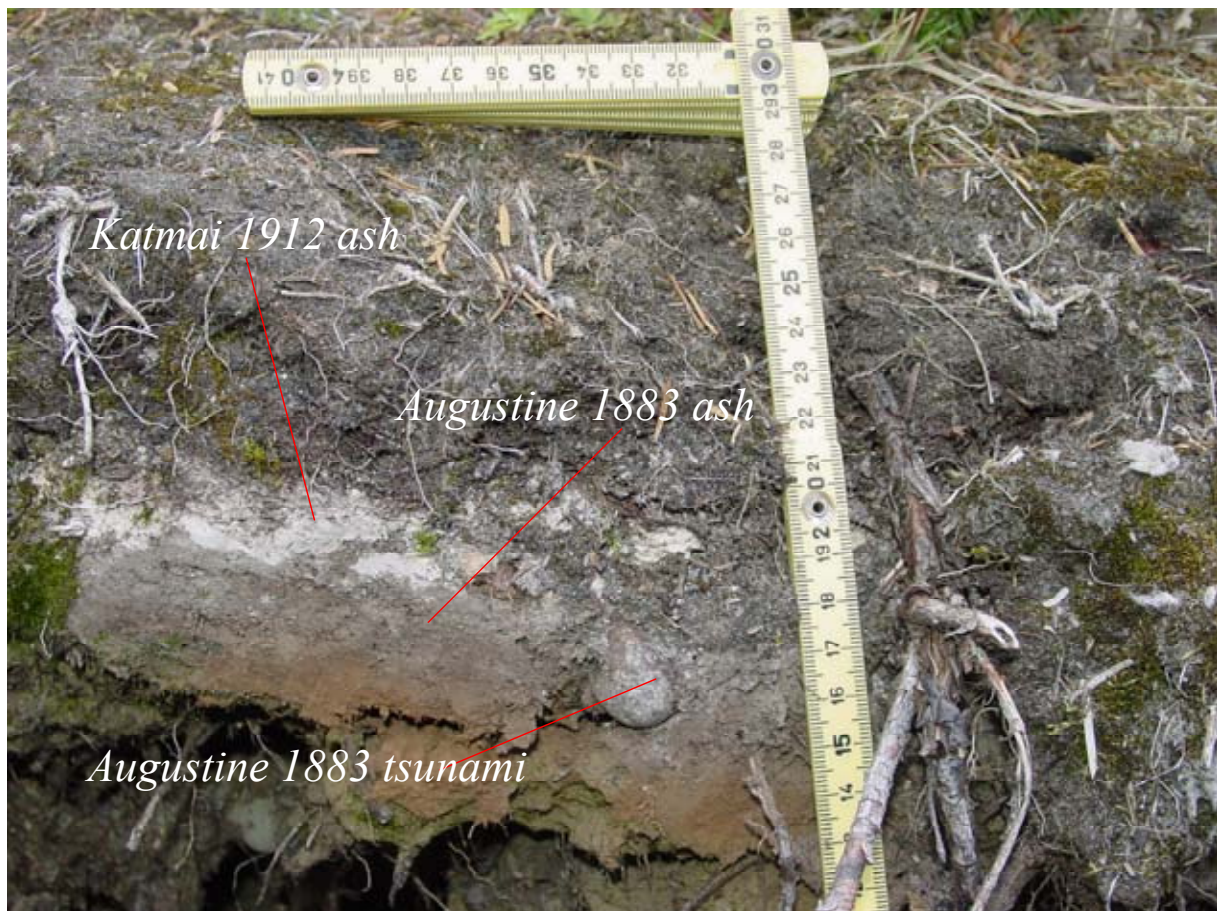

Fig. 5. Paleotsunami deposits near Nanwelak (English Bay), Alaska. Beach cobbles and sand occur in a 1-5 cm thick discontinuous layer overlying poorly developed paleosols, and underlying Augustine 1883 and Katmai 1912 volcanic ash deposits.

4. Summary and Conclusions:

The pattern of dispersal and the magnitudes of tsunami waves which might be potentially generated by a debris avalanche into Cook Inlet from Augustine Volcano indicated by numerical modeling are consistent with geologic evidence of the height and extent of the 1883 Augustine tsunami. An important finding of this work is that, because of the irregular bathymetry around Augustine Island and the geomorphology of surrounding coastlines, significant local amplification of tsunami waves from Augustine Volcano occurs in several areas around lower Cook Inlet. These include the Iliamna coastline on the west side of Cook Inlet, and coastal areas near the small town of English Bay and more developed coastal areas near the towns of Homer and Anchor Point.

References:

Alaska Commercial Company, 1883 [unpublished], Record Books for English Bay Station: Fairbanks, University of Alaska library archives, Box 10 (May 15, 1883-July 1884).

Anders, A., and Beget, J., 1999. Giant Landslides and coeval tsunamis in lower Cook Inlet, Alaska. Geol. Soc. Am. Abst. Prog. V. 31, no. 7, p. A-48.

Beget, J., 2000, Volcanic Tsunamis, in Encyclopedia of Volcanoes ed. H. Siguardsson, p. 1005-1013.

Beget, J., and Kienle, J., 1992, Cyclic Formation of Debris Avalanches at Mount St. Augustine Volcano, Alaska, Nature 356, 701 – 704.

Carey, S., Morelli, D., Sigurdsson, H., and Bronto, S. 2001. Tsunami deposits from major explosive eruptions: An example from the 1883 eruption of Krakatau. Geology 29, 347-50.

Kienle, J., Z. Kowalik, and T. Murty. 1987. Tsunami generated by eruption from Mt. St. Augustine volcano, Alaska. Science 236:1442-1447.

Kienle, J., Kowalik, Z., and Troshina, E. 1966. Propagation and runup tsunami waves generated by Mt. St. Augustine Volcano, Alaska. Science of Tsunami Hazards, 14, 3, 191--206.

Kowalik Z., W. Knight, T. Logan, and P. Whitmore, 2005. Numerical Modeling of the global tsunami: Indonesian Tsunami of 26 December 2004. Science of Tsunami Hazards, Vol. 23, No. 1, 40- 56.

Siebert, L., Beget, J., and Glicken, H. (1995), The 1883 and Late -prehistoric eruptions of Augustine Volcano, Alaska, Journal of Volcanology and Geothermal Research 66, 367 – 395.

Waitt, R. B., and Beget, J., (1996), Provisional Geologic Map of Augustine Volcano, Alaska, U.S. Geol. Survey Open-File Report 96 – 516.

Waythomas, C. F. (2000). Re-evaluation of tsunami formation by debris avalanche at Augustine Volcano, Alaska. Pure and Applied Geophysics 157, 1145-1188.

EXPERIMENTAL MODELING OF TSUNAMI GENERATED BY UNDERWATER LANDSLIDES

Langford P. Sue and Roger I. Nokes
Department of Civil Engineering, University of Canterbury
Christchurch, New Zealand

Roy A. Walters
National Institute for Water and Atmospheric Research
Christchurch, New Zealand

ABSTRACT

Preliminary results from a set of laboratory experiments aimed at producing a high-quality dataset for modeling underwater landslide-induced tsunami are presented. A unique feature of these experiments is the use of a method to measure water surface profiles continuously in both space and time rather than at discrete points. Water levels are obtained using an optical technique based on laser induced fluorescence, which is shown to be comparable in accuracy and resolution to traditional electrical point wave gauges. The ability to capture the spatial variations of the water surface along with the temporal changes has proven to be a powerful tool with which to study the wave generation process.

In the experiments, the landslide density and initial submergence are varied and information of wave heights, lengths, propagation speeds, and shore run-up is measured. The experiments highlight the non-linear interaction between slider kinematics and initial submergence, and the wave field.

The ability to resolve water levels spatially and temporally allows wave potential energy time histories to be calculated. Conversion efficiencies range from 1.1%-5.9% for landslide potential energy into wave potential energy. Rates for conversion between landslide kinetic energy and wave potential energy range between 2.8% and 13.8%.

The wave trough initially generated above the rear end of the landslide propagates in both upstream and downstream directions. The upstream-travelling trough creates the large initial draw-down at the shore. A wave crest generated by the landslide as it decelerates at the bottom of the slope causes the maximum wave run-up height observed at the shore.

1. INTRODUCTION

Tsunami are a fascinating but potentially devastating natural phenomenon that have occurred regularly throughout history along New Zealand's shorelines, and around the world. With increasing populations and the construction of infrastructure in coastal zones, the effect of these large waves has become a major concern. There are several reasons tsunami are hazardous. Firstly it is their size, with waves several hundred metres in height known to have occurred in the past (Murty 2003; New Scientist 2004). The highest recorded wave run-up was generated in 1958 following a sub-aerial landslide in Lituya Bay, Alaska. This impulse wave caused deforestation and soil erosion down to bedrock level to an elevation of 524 m, and has been modeled experimentally by Fritz et al (2001). Secondly, tsunami can travel at considerable speeds, upwards of many hundreds of kilometres per hour. Lastly, tsunami occurrences are unpredictable. Seismic events such as earthquakes and landslides, the generation mechanisms of tsunami, occur sporadically in time and space, and not all seismic events have generated significant waves. Studies of historical records and forensic analysis of coastal geology have shown significant wave events occur frequently across the world. Many natural phenomena are capable of creating tsunamis. Of particular concern is the underwater landslide-induced tsunami, due to the potentially short warning before waves reach the shore. Sections of sediment or rock on the seabed can slide into deeper water, and this movement translates into a disturbance on the water surface above.

Experimental research into submarine landslide-induced tsunami began in 1955 to dispel the belief of many at the time that disturbances such as submarine landslides were unlikely to cause tsunami. The type of submarine mass failure is based on the landslide geometry and on the characteristics of the failure material, such as chemical composition, grain size, and density. Due to the inherent difficulties with scaling of these factors, the landslide failure mass is often approximated experimentally by a solid mass, either triangular or semi-elliptical in shape.

Wiegel (1955) preferred to experiment with sliding and falling blocks of various shapes, sizes, and densities, as opposed to granular slide experiments. These two-dimensional tests were performed in a constant depth channel, and factors such as initial submergence, slide angle, and water depth were varied, and the wave characteristics were measured using parallel-wire resistance wave gauges at both near and far field locations. Surface time histories of the tests downstream of the disturbance showed a crest formed first, followed by a trough with amplitude one to three times that of the first crest, and followed by a crest with a similar magnitude to the trough. It was found that dispersive waves were generated, as crests and troughs continued to be generated with increasing distance, and the amplitudes of the waves diminished as they propagated. The magnitude of the wave heights were found to depend primarily on the block weight, initial submergence, and water depth. The period of the waves was found to increase with increasing block length and decreasing incline angle. A dimensional analysis concluded that no parameters could be neglected. Instead, certain parameters were found to be related in such a way that it was not possible to hold all but one constant to determine their individual effects. Computations indicated approximately 1% of the initial net submerged potential energy of the sliding block was transferred into wave energy, with this percentage increasing with reduced initial submergence and decreasing water depth.

Other experimentalists have chosen to simulate a submarine landslide with a right-triangular prism sliding down a 45° slope (Rzadkiewicz et al. 1997; Watts 1997; Watts 1998; Watts 2000; Watts and Grilli 2003). The two-dimensional experiments of Rzadkiewicz et al. (1997) were a short series of tests to produce data to compare directly with some of their numerical models. These tests involved right-triangular simulated landslide masses, consisting of solid material, and granular sand and gravel, sliding down 30° and 45° slopes. Side-on images were captured at 0.4 s and 0.8 s after slide release, and from these landslide material shape and water level profiles were determined.

Watts' (1997) experiments were similar, consisting of solid and granular slides along a 45° slope. However, a wider parameter space was investigated, with slide material, initial submergence, porosity, and

density varied. Resistance wave gauges were used to measure water level time-histories at various locations downstream of the slide, and a micro-accelerometer recorded the landslide's centre-of-mass motion. A comparison of the motions of granular slide material with the motions of a solid block, by using a variety of granular materials to simulate the landslide failure mass, found that the centre of mass motion of a granular slide was similar to that of a solid block slider. This study also tried to develop a non-dimensional framework in which to predict maximum wave amplitudes (wave troughs) from specific landslide parameters such as landslide length and initial submergence.

Some of the later experimental research is in three-dimensional wave experiments with both angular, semi-hemispherical (Liu et al. 2005; Raichlen and Synolakis 2003), and streamlined solid block slider shapes (Enet et al. 2003). The large-scale tests of Raichlen and Synolakis (2003), attempting to minimise the effects of viscosity and capillary action, consisted of a 91 cm long, 46 cm high, and 61 cm wide triangular wedge-shaped block sliding down a planar (1 V:2 H) slope. The 475.52 kg block started its slide at various submergences from fully submerged to partially aerial. A micro-accelerometer and position indicator recorded the block location time-histories, and an array of resistance wave gauges recorded the propagating waves and run-up heights on the beach behind the sliding mass. The three-dimensional simulated submarine landslide tests of Enet et al. (2003) were developed to produce experimental data suitable for comparison with their numerical model results. The flattened dome-like slider block had a thickness of 80 mm, a length of 400 mm, a width of 700 mm, and a bulk density of 2,700 kg/m^3. The initial submergence was varied and its motions as it slid down the 15° slope were recorded with a micro-accelerometer located at the block's centre-of-mass. The propagating wave field generated was measured with an array of four capacitance wave gauges.

In an effort to produce comparable results from their numerical models, the international tsunami research community defined a benchmark configuration for studying the generation of tsunami by underwater landslides. This was deemed necessary due to the difficulties in interpreting the results from the various experimental and numerical models incorporating a wide range of constitutive behaviours (Grilli et al. 2003; Watts et al. 2001). It was also noted that the sharp edges of the triangular sliding blocks used in previous experimental studies were difficult to model computationally due to the strong flow separation at the vertices. Apart from reef platform failures, this shape was considered to be unrepresentative of the geometry of most underwater mass failures. The tsunami community's recommendation was for a smoother, more streamlined shape which, despite its idealisation, would represent the majority of real events (Grilli et al. 2003).

Two-dimensional tests were recommended as they presented fewer difficulties than three-dimensional tests for numerical modeling. The benchmark configuration consisted of a semi-elliptical block sliding down a planar slope at 15° from the horizontal. The landslide had a thickness:length ratio of 1:20 and a specific gravity of 1.85. It was completely submerged, with the centre of the top surface initially submerged 0.259 times the length of the landslide. A basic set of experiments with this arrangement was performed, but the quality of the results were inadequate to validate numerical models due to electrical point wave gauge accuracy (Watts et al. 2001).

The work of Fleming et al (2005) also experimented with this benchmark configuration. Sets of experiments were performed with a semi-elliptical block and water levels were recorded with three resistance wave gauges. The data generated was to be compared with the results of Watts et al (2001). Further experiments with triangular solid and granular slides were completed to examine the effects of initial landslide shape, initial submergence, volume, density, and deformability. Water levels in the near- and far-field were measured with an array of five wave gauges.

Experimental laboratory test results are generated using grossly simplified geometries and are inherently difficult to scale up to full-size. To model each tsunami scenario in the laboratory at sufficient scale and complexity to account for landslide deformations and ocean bathymetry would prove to be extremely costly. As such, laboratory experiments are used to observe specific features of tsunami generated

by sliding masses in a controlled manner, and numerical models take into account the various shoreline and deep-ocean geometries when used to predict full-sized events.

A variety of computational models have been developed by researchers to look at the many different phenomena associated with submarine landslides and tsunami. Each model makes certain assumptions in order to simplify the governing equations of fluid dynamics. These assumptions are associated with fluid viscosity, landslide friction, and wave linearity. There are models for slope failure (Martel 2004), landslide and water interaction (Jiang and Leblond 1992), wave generation and propagation (Enet et al. 2003; Grilli et al. 2002), and wave run-up (Kanoglu 2003; Kennedy et al. 2000; Liu et al. 2005; Synolakis 1987; Tarman and Kanoglu 2003; Walters 2003). Most models use a finite or boundary element approach (Grilli et al. 2002; Mariotti and Heinrich 1999; Rzadkiewicz et al. 1997).

The more complex models are able to predict fluid parameters such as water level, wave run-up, and sub-surface velocities and pressures, varying in three spatial dimensions and over time. There are also several simple methods for predicting gross wave properties, such as maximum expected wave heights. Murty (2003) used information available in the literature to find a simple empirical linear relationship between landslide volume and the maximum observed wave heights. Another simplified model, used to couple the landslide mass to the generated waves, was to determine the amount of energy transferred from the block's initial gravitational potential energy to the potential energy of the waves. This is found to be of the order of 1% - 2% (Jiang and Leblond 1992; Ruff 2003; Tinti and Bortolucci 2000; Watts 1997).

Wave run-up at planar beaches has been studied in significant detail in the past (Kanoglu 2003; Kennedy et al. 2000; Liu et al. 2005; Synolakis 1987; Tarman and Kanoglu 2003; Walters 2003). These models studied run-up from waves generated from distant sources and looked at their transformation, breaking, and run-up as they approached the shore. In an underwater landslide, the failure mass motion will be away from shore, generating waves that also move offshore. However, little work has looked at the wave run-up at the beach behind the landslide, as it is this that is of immediate danger to the population and infrastructure in the proximity of the slide.

Individual models are tested using different geometries and motions, which make comparisons between models difficult (Grilli et al. 2002; Grilli and Watts 1999; Mariotti and Heinrich 1999; Rzadkiewicz et al. 1997). Also, many of these models have been developed in isolation from submarine landslide geomorphology, and are therefore difficult to apply to real situations. Even when there are large amounts of field data available to validate these models, such as from the 1998 Papua New Guinea event, there are difficulties and controversies plaguing their interpretation (Davies et al. 2003; Imamura and Hashi 2003; Lynett et al. 2003; Okal 2003; Satake and Tanioka 2003; Tappin et al. 2003; Tappin et al. 2001). Experimental tests are a means to validate these numerical models. To some extent validated models possess some predictive qualities.

The following sections contain information pertaining to the laboratory experiments conducted at the University of Canterbury. Details of the experimental set-up are given in Section 2, along with information on the methods developed to measure the wave phenomena. Some preliminary results are given and discussed in Section 3, followed by some concluding remarks in Section 4. Further details regarding the experimental methods can be found in Sue et al (2006). Additional results from the experimental tests will be included in future papers, with full results and numerical model comparisons to be included in Sue (in preparation).

2. METHODS

The motivation behind this experimental programme was to generate a comprehensive dataset using the benchmark configuration defined by the international tsunami research community (Grilli et al. 2003; Watts et al. 2001). The data from this study would be of sufficient quality for comparisons with numerical models. The same two-dimensional configuration as Watts et al (2001) was used. This consisted of a model landslide with a thickness:length ratio of 1:20. However, unlike their experiments, a variety of landslide densities and initial submergences were investigated here.

The following sections describe the experimental programme and set-up. This is followed by information on the Particle Tracking Velocimetry (PTV) technique used to measure the landslide kinematics. The development of the Laser Induced Fluorescence (LIF) technique, to measure the water levels, is also presented along with details of its capabilities compared with traditional electrical wave gauges.

2.1 EXPERIMENTAL PROGRAMME

An experimental programme was completed to measure the landslide motions and wave fields generated by laboratory underwater landslides with fifteen combinations of specific gravity and initial submergence. Specific gravity is defined as the ratio of the total unsubmerged mass of the block, m_b, and the mass of water displaced by the landslide, m_o, as shown in Equation 1.

$$\text{specific gravity} = m_b / m_o \qquad \textbf{(1)}$$

Equation 2 defines the non-dimensional initial submergence as the ratio of the depth of water directly above the landslide centre of mass at its initial starting position, d, and the length of the landslide block along the slope, b. A diagram of the experimental set-up is included in Figure 1.

$$\text{initial submergence} = d / b$$
$$\textbf{(2)}$$

The testing programme consisted of a model landslide block with a combination of five different specific gravities and five initial submergences, as presented in Table 1. Test SG5-IS5 combined the highest specific gravity with the shallowest initial submergence, and produced the largest water level response. SG5-IS1 combined the heaviest specific gravity with the deepest submergence, while SG1-IS5 combined the lightest specific gravity with the shallowest submergence, and both of these produced some of the smallest responses. A range of combinations was not tested as they were expected to create small waves and suffer from resolution issues. The repeatability of the experimental techniques were rigorously assessed, details of which have not been included here, but appear in Sue et al (2006). Test repeatability was important because it allowed different testing methods to be used sequentially, instead of simultaneously, resulting in reduced experimental complexity.

Table 1. Experimental test combinations of Specific Gravity (SG) and Initial Submergence (IS).

Specific Gravity:						
5 variations		Lightest	SG1	1.63		
			SG2	2.23		
			SG3	2.83		
			SG4	3.42		
		Heaviest	SG5	4.02		
			SG = Specific Gravity			
Initial Submergence:						
5 variations		Deepest	IS1	0.5	d/b	
			IS2	0.4	d/b	
			IS3	0.3	d/b	
			IS4	0.2	d/b	
		Shallowest	IS5	0.1	d/b	
			IS = Initial Submergence			
			d = depth of water above landslide CoM			
			b = block length (500mm)			
Combinations tested:						
		IS5	IS4	IS3	IS2	IS1
	SG5	*	*	*	*	*
	SG4	*	*	*	*	
	SG3	*	*	*		
	SG2	*	*			
	SG1	*				

2.2 EXPERIMENTAL SET-UP

The wave tank used in these experiments was a 0.250 m wide, 0.505 m deep, and 14.7 m long flume in the University of Canterbury's Fluid Mechanics Laboratory. The tank was filled with tap water to a depth of 435 mm. This flume was housed in a room with all windows and other openings blacked out to reduce outside light interference and to contain the laser light when it was operating in the darkened room.

An inclined ramp at an angle of 15° to the horizontal was placed at one end of the flume, and strips of stainless steel and PVC sheeting were imbedded into the surface of the slope. The mildly flexible stainless steel strips were used to provide a means for the surface of the slope to transition smoothly from the 15° slope to the horizontal floor of the flume, and allow the landslide to slide down the slope and then along the floor where it would eventually stop due to friction. Profiles of the curved steel strips were cut from acrylic and fixed underneath to provide rigid support. The PVC strips were used to provide a more slippery surface upon which the landslide would slide compared to the acrylic and stainless steel base material, and could be easily replaced when worn.

The prismatic semi-elliptical model landslide was milled from a solid block of aluminium. The block length, b, was 0.5 m (major axis length) and was 0.026 m thick (minor axis = 0.052 m), and 0.25 m wide. The total volume of the block was 2.419 litres. Hollow cavities were incorporated into the base of the block that could be filled with polystyrene or lead shot ballast to vary the total specific gravity of the landslide. A plastic sheet was screwed into place to cover the cavities and secure the ballast. To minimise the reflectivity, the landslide block was painted matt black. A photograph of the aluminium slider block is included in Figure 1. To further minimise the sliding friction, 3 mm diameter hardened steel balls were embedded into the base of the block, at the four corners along the leading and trailing edges. To lubricate the steel balls and PVC strips, silicone grease was applied to the slope surface. A length of fishing line, attached to the trailing edge of the block, was used to anchor the block to the release mechanism and hold it at the correct initial submergence prior to each experimental run. Different submergences were achieved by using different lengths of fishing line.

Initial investigations showed that the wave field generated was highly dependent on the stopping mechanism, and previous experimentalists failed to note what technique they used to stop their sliding blocks when they reached the bottom of the slope. It is assumed that the blocks just topple over and stop when they reach the end of the slope, and their wave records end before this time. For heavier blocks with high accelerations and velocities, these times can be quite short. This does not allow sufficient time to observe the waves as they develop and propagate. To see the effect abruptly stopping the block at the toe of the slope had on the wave field, a tether was attached to the landslide that was just long enough for the block to slide normally from its initial position until the end of the slope. It was found that a block coming to a sudden stop created waves larger than the waves that were generated by the landslide if it were sliding and decelerating naturally. It was considered desirable that the landslide be allowed to progressively transition from sliding down the slope to run out on the flume floor of its own accord. This minimised the waves being generated by the sudden stopping of the block, and was considered to more closely represent the deposition of actual underwater landslide masses sliding along shallow slopes.

2.3 EXPERIMENTAL TECHNIQUES

In this experimental programme, PTV was used to measure the motions of the landslide block as it slid down the slope. The PTV software used in this experimental program was FluidStream (Nokes 2005a), developed at the University of Canterbury for flow visualisation. White plastic sheeting was placed behind the flume to provide a white background. Fluorescent tube lights in the room and a halogen spotlight were used to illuminate the landslide. A series of red dots were applied to the side of the black coloured model landslide and a Canon MV30i colour digital video camera recorded the block's motion against the white background. Image sequences were captured and recorded to a computer using Adobe Premiere software. Image processing software was used to isolate the red dots from the black and white background of the white plastic sheeting and the black landslide. The PTV software was then used to track the red dot at the landslide centre of mass through the image sequence. The entire slope was too large to capture with adequate resolution from one camera placement so several camera positions were used and the landslide positions from each location were combined.

The use of electrical point wave gauges at specific locations can only give limited insights into the wave generation process, as the spatial changes in water profile between the gauge positions are not measured. There are also questions as to the influence of surface tension and meniscus effects on the gauge wires at the small laboratory scales, as well as the effect of having objects physically in the flow. To remedy this, a non-intrusive water level measurement technique was developed that minimised the disturbance to the water, and also captured the spatial as well as the temporal variations.

Recording water levels optically has many advantages over stationary point wave gauges, the main one being its ability to capture the spatial variation of the waves as well as the temporal variations. To avoid the menisci problems associated with recording the water levels at the sidewalls under ambient light conditions, a LIF technique was developed to capture the wave profiles and wave run-up heights away from the sidewalls. A small concentration of rhodamine 6G fluorescent dye was stirred into the flume water, and illuminated with a 1.0 W vertical laser light sheet orientated parallel with the longitudinal axis of the wave tank. The 0.1 mg/L dye concentration in the water column fluoresced due to excitation by the laser light, and this contrasted with the surrounding darkness of the blackened room. A high-resolution digital video camera was used to record a series of images of the illuminated water. In each frame the interface between the regions of high and low light intensity marked the location of the free surface. A diagram of the experimental set-up is shown in Figure 1. The camera used to capture images of the free surface response to the release of the model landslide was a Pulnix TM1010 monochromatic progressive scan camera with a 1008 x 1008 pixel resolution. An orange-colour filter was used to filter out the laser light from the fluorescent light. Image sequences were recorded at 15 Hz and were archived to computer hard disc as a series of JPEG images. To eliminate the interference of the water line at the sidewall nearest the camera, the

camera was mounted slightly higher than the water level to capture the water surface in the illuminated plane. This was taken into account in the analysis of the recorded images.
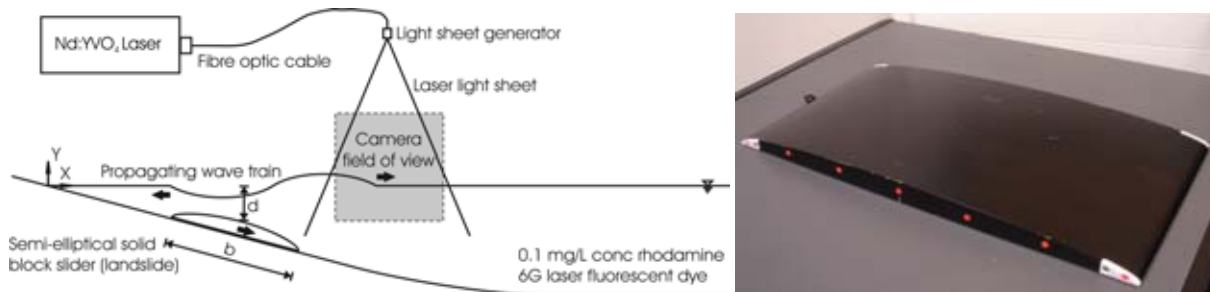

Figure 1. Experimental set-up for LIF water level recording of submarine landslide-induced tsunami, and a photograph of the model landslide.

ImageStream (Nokes 2005b), an image processing software package developed at the University of Canterbury, was used to determine the light intensity of each pixel in each of the JPEG images. The transition from the high intensity light of the fluorescing water to the low light intensity of the air signalled the location of the water surface. Sub-pixel resolution was achieved through a simple intensity interpolation process. The water levels were corrected for refraction and parallax errors, and a simple scaling procedure then transformed the water level from pixel space to physical space. Further details of the LIF technique and the analysis process are presented in Sue et al (2006).

To observe a substantial length of water surface with adequate resolution, the single camera was used to observe the flow in different locations for repeated runs of the same experiment. The camera and laser sheet were placed at the shoreline to record the propagation of the landslide-generated waves up the slope. The camera and light sheet were then moved further downstream to observe the downstream propagation and continued evolution of the waves. The water profiles were then combined to create a wide field of view of the surface response. The water surface profile experiments used 31 consecutive camera positions to record water levels from approximately 0.3 m upstream of the original shoreline to 10.1 m downstream.

To compare the performance of the LIF technique with traditional wave gauge methods, several tests were performed with both the LIF and point wave gauges operating simultaneously. Three Churchill Controls resistance wave gauges (RWG) were placed parallel to the laser sheet in the region above the base of the slope, approximately 0.145 m apart. The gauges were placed behind the light sheet so that they did not obscure the fluorescing water surface from the camera. Point LIF water level readings were determined at the same positions as the resistance wave gauges, and the two records compared. Tests in which large, moderate and very small waves were created were used to compare the two techniques. As illustrated in Figure 2, the LIF method produced point measurements of water level comparable to those of the RWGs. Note that each horizontal gridline represents two pixels in the plot of the largest waves, and one pixel in the small wave height plot.
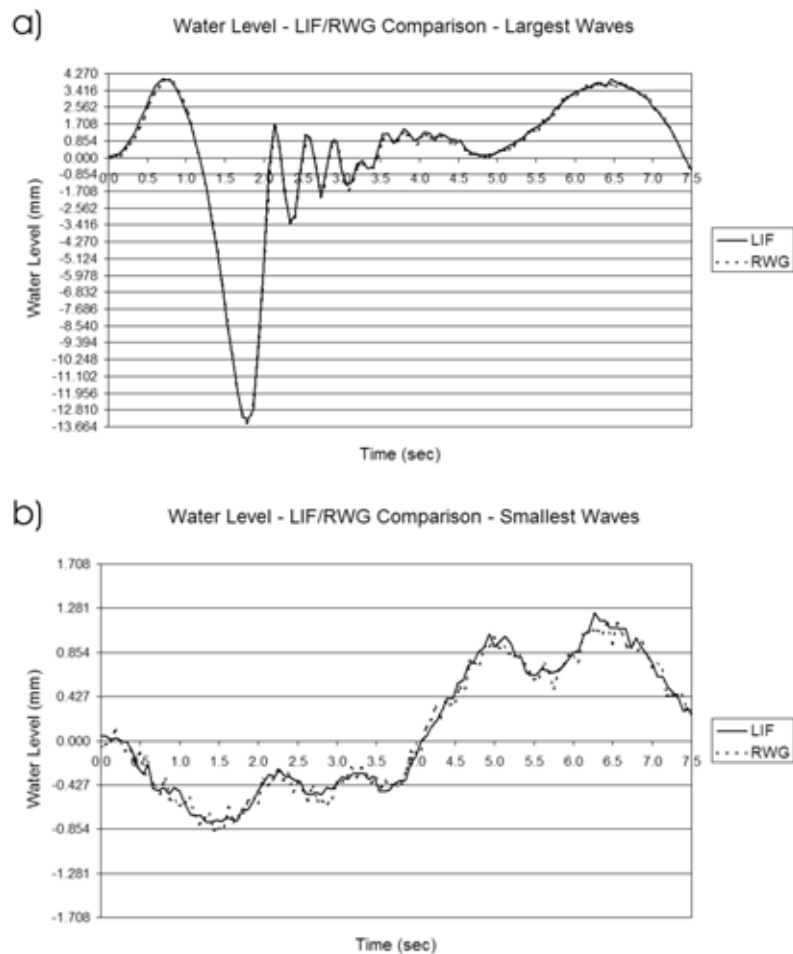
a)

b)

Figure 2. Plots of LIF and RWG for comparison of performance for large and small wave heights. Note the different gridline intervals, as one pixel = 0.427 mm.

3. EXPERIMENTAL RESULTS AND DISCUSSION

This section presents preliminary results from the experimental programme. It begins with details of the landslide kinematics, such as maximum landslide velocity and initial acceleration. Results from the water level measurements of wave amplitudes and run-up/down are then discussed. The percentage conversion of landslide potential energy into other forms of energy concludes this section. Some of the data presented in this section has been non-dimensionalised. Lengths such as water levels, run-up heights, and downstream positions have been non-dimensionalised by the landslide length, b. Accelerations have been non-dimensionalised by the gravitational acceleration, g, and times by $\sqrt{(g/b)}$.

3.1 LANDSLIDE KINEMATICS

An example of the landslide centre of mass velocity time history is shown in Figure 3 for the SG3_IS5 combination. The landslide velocity increases almost linearly from rest and reaches a maximum at the bottom of the slope, at which point the block slows and comes to rest along the flume floor. As indicated

by the increasing velocity of the landslide at the toe of the slope, terminal velocity is not reached. Velocity time histories for other combinations exhibited similar behaviour. This can be contrasted with the slider motions of Watts (1997), in which his landslides rapidly reached terminal velocity. Figure 3 also shows a time history plot of the landslide centre of mass acceleration for the SG3_IS5 test. The form of the acceleration plot is similar for all the specific gravity and initial submergence combinations, with only the magnitude and timing of the accelerations differing. The rapid increase to the peak acceleration typically occurs within two camera frames, or 0.133 seconds. Initial acceleration is taken as this peak value. The acceleration decreases slightly as the landslide progresses down the slope, before a rapid deceleration as the block reaches the base of the slope and transitions to sliding along the flume floor. A phase of roughly constant deceleration occurs as the landslide slows and finally stops. During the landslide experiments of Watts (1997), the accelerations peaked almost instantaneously before rapidly decreasing as the block approached terminal velocity. His acceleration time histories were typically measured for durations of 0.6 seconds.
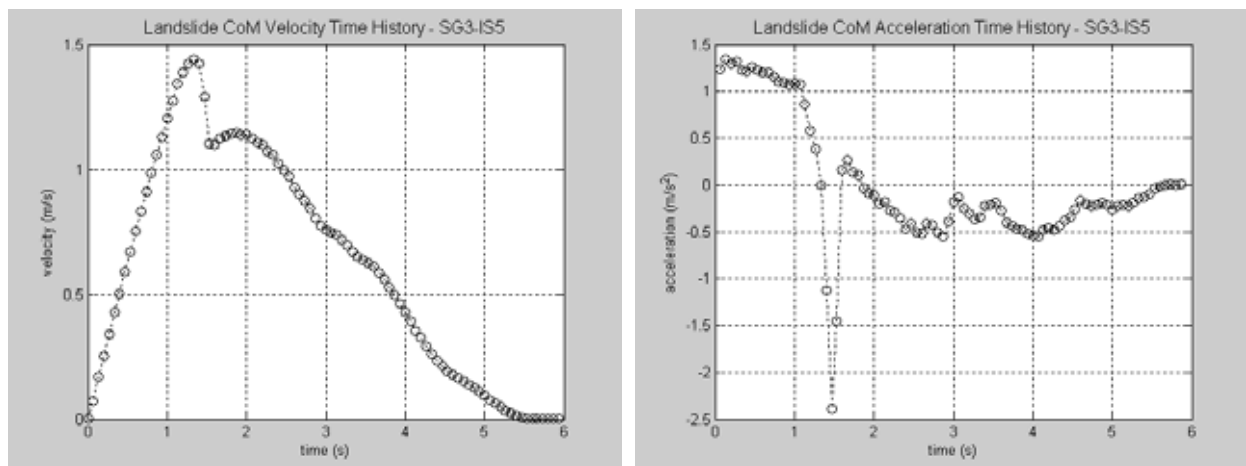

Figure 3. Landslide centre of mass velocity and acceleration time histories for SG3_IS5 test.

3.2 WAVE FIELDS

The evolution of the waves through space and time can be observed by looking at the water surface profiles. The changes in the lengths and total number of waves can be inspected. Figure 4 shows the water surface profiles of the SG3_IS5 test at successive times between 0.600 s and 5.600 s. Present in the first frame at time = 0.600 s is the 1st crest, 1st trough, and the beginnings of the 2nd crest, propagating downstream. The solid black bars indicate the approximate position of the landslide. The wave trough causing the run-down observed at the beach is also present as a trough propagating upstream. The following frames illustrate the evolution of these waves as they propagate. The 1st crest amplitude continues to increase initially, peaks, and then gradually decreases as the wave enters deeper water and its wavelength increases. The 1st trough and 2nd crest also exhibit this behaviour, although at later times. The continual generation of small amplitude waves with short wavelengths at the upstream end creates a propagating wave packet.
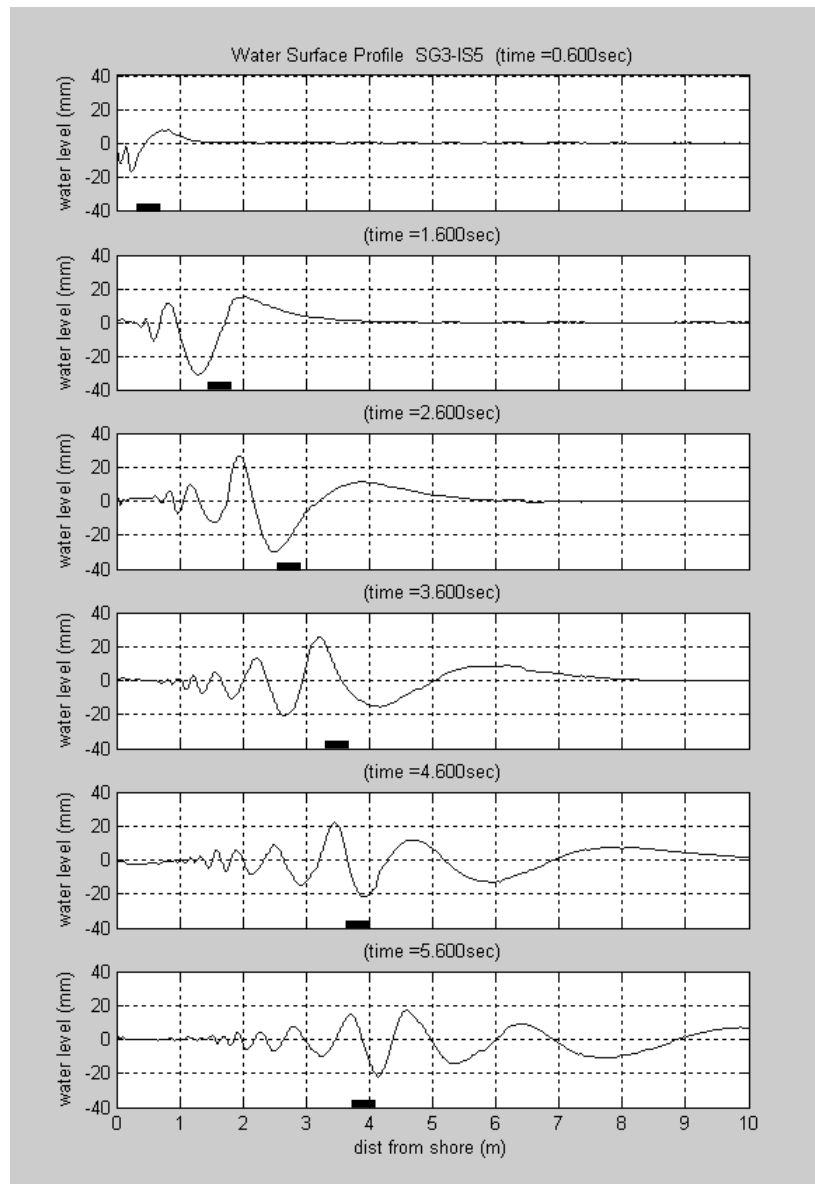
Figure 4. Water surface profiles at time = 0.600, 1.600, 2.600, 3.600, 4.600, and 5.600 seconds for SG3_IS5 test. The solid black bars indicate the approximate position of the landslide.

The water level profiles in Figures 4 are presented in a continuous manner in Figure 5. The plot in this figure displays water level, on the vertical axis, against time and downstream position on the horizontal axes. The red colours indicate positive water levels, or wave crests, and blue represents the negative water levels of troughs. The partially obscured black line indicates the downstream position of the landslide centre of mass. The evolution of the waves and the generation of the wave train are clearly illustrated. Figure 6 plots the three-dimensional water level data on a two-dimensional contour plot. In this form the wave propagation speeds are more clearly seen. The wave speeds relative to the landslide are also illustrated. From this plot it can be seen that the 1st crest forms ahead of the landslide centre of mass and the 1st trough forms behind it. The point at which these two waveforms meet follows the landslide centre of mass as it slides down the slope.
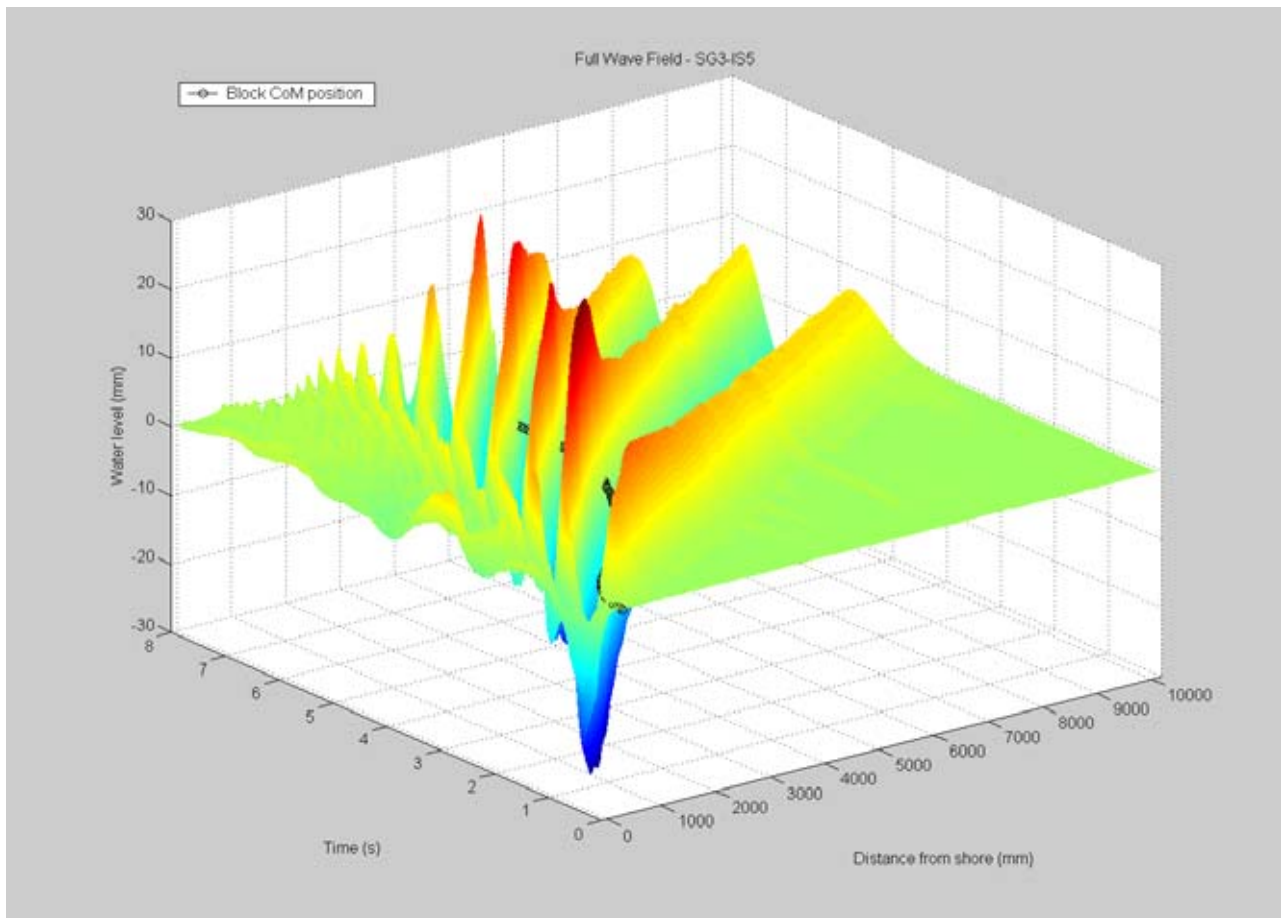
Figure 5. Oblique three-dimensional views of water surface profile time history for the SG3-IS5 test.

At this point, a qualitative description of the wave generation processes illustrated in two-dimensional contour plots of all fifteen combinations is given. The motion of the landslide generates the 1st crest as it pushes up the water ahead of it. The acceleration of the surrounding fluid creates a water pressure distribution over the moving landslide. The high pressures ahead of the landslide forces up the water surface above it to form the 1st wave crest. This crest is not attached to the landslide and propagates freely once generated. The accelerating fluid and the turbulent wake above and behind the sliding block creates a region of low pressure. This low pressure pulls the water surface down to form a depression. This wave trough is forced to propagate at the same speed as the accelerating landslide due to the low pressure region being directly connected to the sliding block. The 1st trough is free to propagate once the landslide reaches the bottom of the slope and begins to slow. The decrease in velocity of the block disrupts the low pressure region, and its connection with the trough can not be maintained.

Dispersion effects are also present, noticeable as the progressively slower speeds of waves further back in the wave train. The continual generation of waves at the trailing end of the train is also visible. The region of generation of these waves moves downstream over time. As individual waves are generated, their speeds increase as they move into deeper water. Also noticeable is the weak signal of disturbances propagating upstream of the slider, especially early in the wave generation process. These waves ultimately form the run-up and run-down observed at the shore.
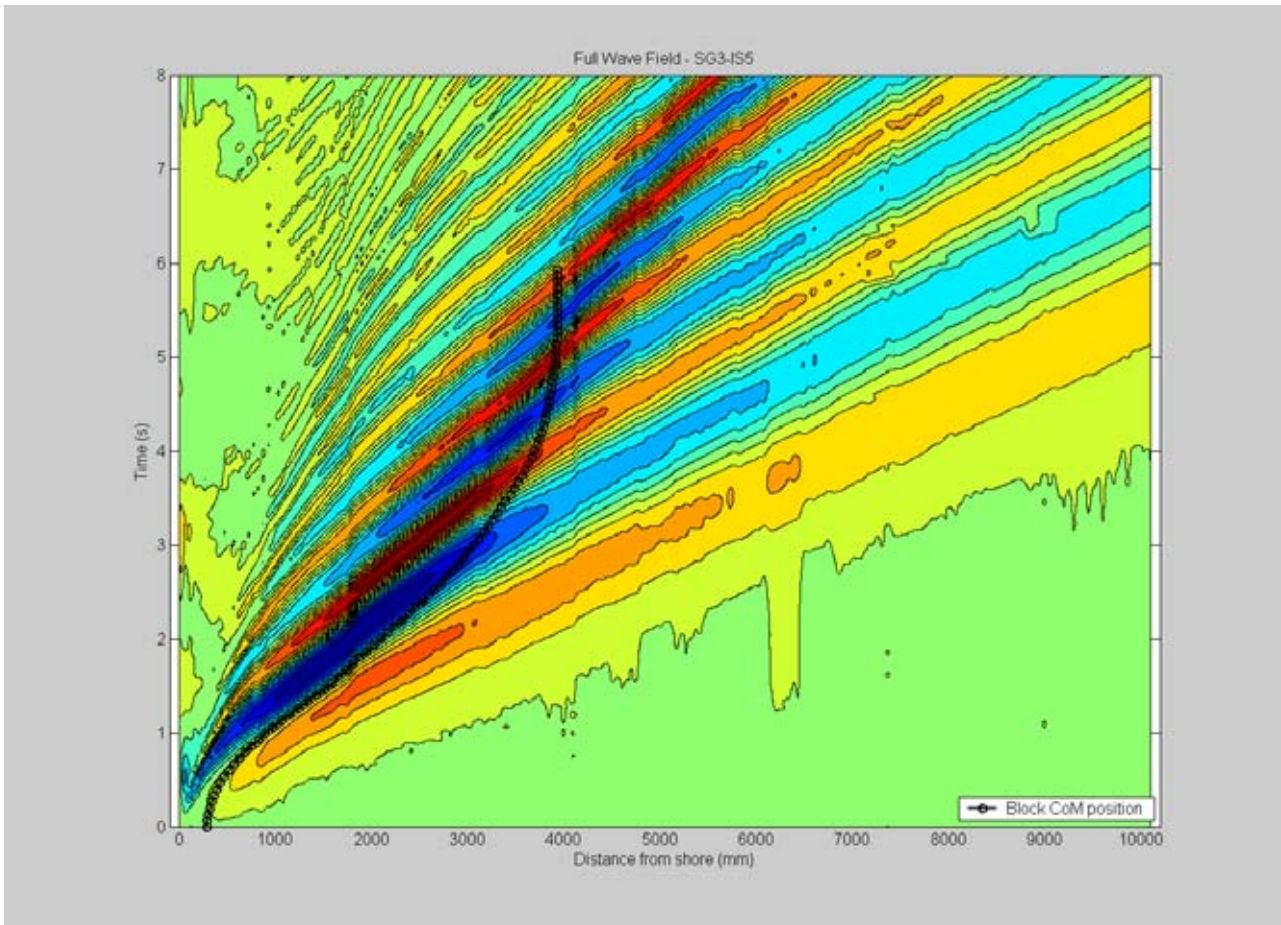
Figure 6. Two-dimensional contour plot of water surface profile time history for the SG3-IS5 test. Red colours indicate wave crests and blue colours indicate wave troughs. Note the various wave speeds present within the wave train.

The overall maximum crest amplitude and overall maximum trough amplitude for the fifteen test combinations are presented in Figure 7. These plots illustrate the increase in maximum crest and trough amplitude with heavier specific gravities and shallower initial submergences.
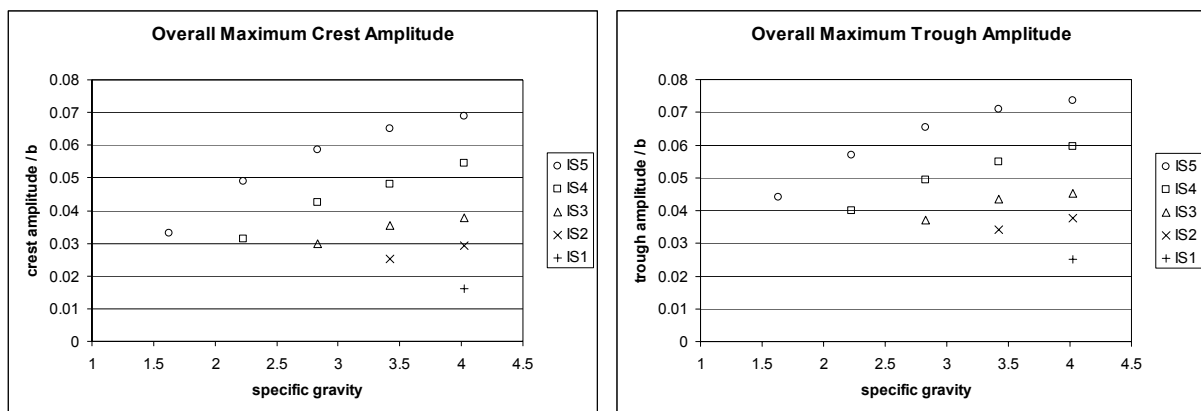

Figure 7. Overall maximum crest amplitude and overall maximum trough amplitude as a function of specific gravity.

The extent of wave run-up and run-down at the shore are also important parameters, as it is the wave magnitudes at the shore that are of immediate concern in practical situations. Indications of the likely draw-down and wave inundation, as well as the times at which these occur, are useful for communities with assets situated in the coastal area. Wave run-up and run-down heights along the slope were measured vertically from the original still water level. A typical wave run-up/down height time history is presented in Figure 8 for test SG3_IS5. The key features of this time history, and of those for other specific gravity and initial submergence combinations, is the large initial draw-down followed by a rebound to a level close to the original water level. This is followed by a positive run-up and relaxation back to the original mean water level.
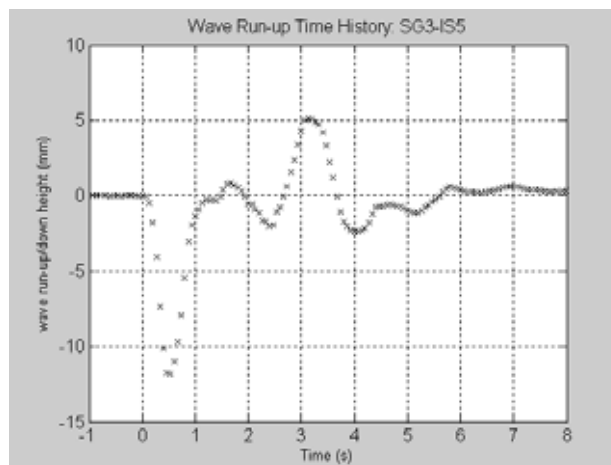

Figure 8. Wave run-up/down height time history for the SG3_IS5 test.

The trends observed in the maximum non-dimensional wave run-up data presented in Figure 9 indicate that the maximum wave run-up heights increase for heavier specific gravities and shallower initial submergences. We suggest that the positive run-up peak occurs as a result of a wave generated by the short duration, but high magnitude, deceleration of the landslide upon reaching the base of the slope. The wave generated at this point and time propagates upstream and runs up the slope. To provide further evidence of the landslide deceleration origins of the run-up height observed, Figure 9 also plots maximum non-dimensional wave run-up heights against maximum non-dimensional landslide decelerations at the base of the slope. The data from all fifteen combinations collapses onto one curve when the maximum deceleration is used as the independent variable.

Preliminary tests with the landslide block tethered so that it abruptly stopped at the base of the slope, resulted in the generation of waves with amplitudes larger than those initially generated by the accelerating landslide. The removal of the tether and allowing the landslide to slow naturally along the flume floor resulted in a significant reduction in the magnitude of the wave generated by the slowing block. However, the maximum positive run-up height was still dominated by the run-up of this landslide deceleration-induced wave. This indicates that landslide deceleration can have a significant affect on the magnitudes of the observed wave run-up.
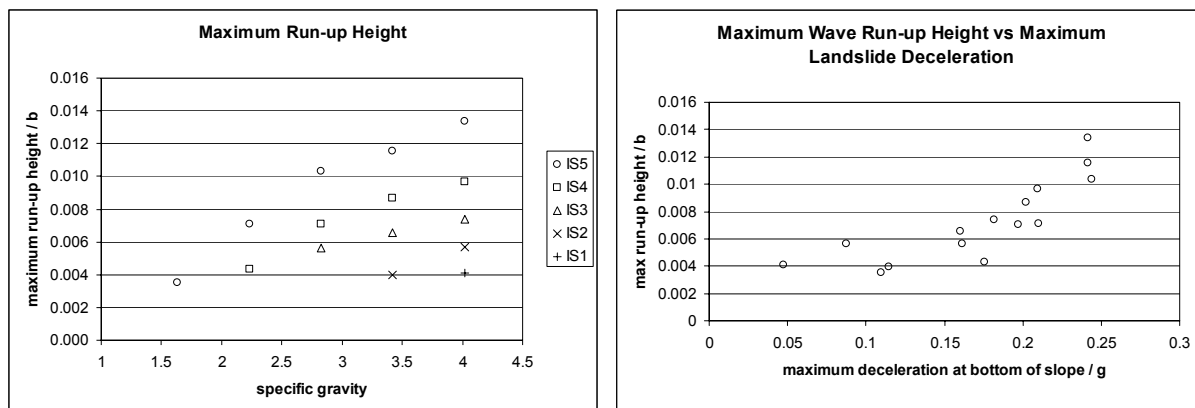
Figure 9. Maximum wave run-up height as functions of specific gravity and maximum deceleration of the landslide at the base of the slope.

Figure 10 indicates that the non-dimensional time of maximum run-up occurs earlier for higher specific gravities and deeper initial submergences. The added mass and shorter slope distances cause the landslide to reach the base of the slope earlier. As the run-up peak is most likely created by the deceleration of the block at toe of the slope, the maximum run-up occurs earlier. Based on this theory, the travel time for a wave generated above the toe of the slope to travel back to the beach was calculated. A wavelength of 0.5 m, equal to the length of the landslide, was assumed and the time for this wave to propagate upstream to the shore was added to the time for the landslide to reach the base of the slope. The ratio of the measured times to the calculated times of maximum run-up for all fifteen test combinations are very close to unity, and are plotted in Figure 10.
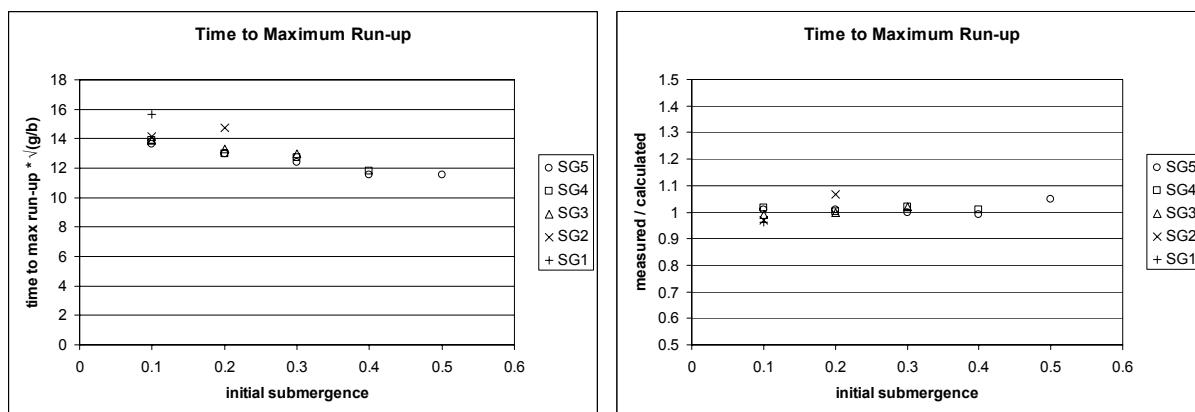

Figure 10. Time of occurrence of maximum wave run-up height and a comparison of measured and calculated values, assuming a 0.5m wavelength crest was generated above the toe of the slope and propagated upstream, as a function of initial submergence.

The magnitude of the non-dimensional wave run-down observed at the shore decreases with lighter specific gravities and deeper initial submergences, as shown in Figure 11. The wave run-down and the 1st wave trough are formed by the same mechanism, namely the initial draw-down of the water surface above the landslide. The depression that forms over the rear end of the block propagates in both the upstream direction, to cause the large initial draw-down at the shoreline, and downstream as the 1st wave trough. The magnitudes of these two parameters are governed by the strength of this initial water surface depression.

The correlation between the maximum run-down height and the maximum 1st wave trough amplitude, as shown in Figure 11, tends to confirm the common origin of these two phenomena.
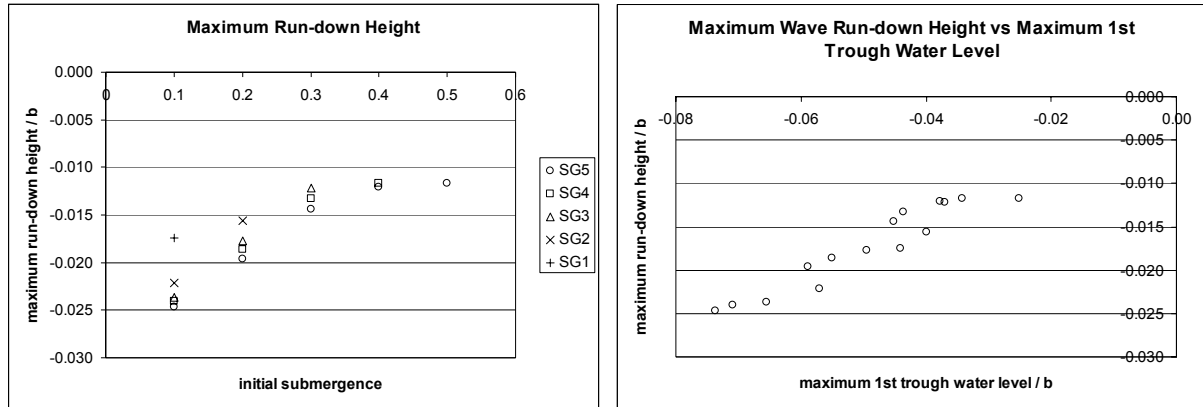

Figure 11. Maximum wave run-down height as functions of specific gravity and maximum 1st trough amplitude.

As shown in Figure 12, the non-dimensional time the maximum wave run-down occurs is independent of specific gravity, dependent solely on the initial submergence of the landslide. The maximum run-down occurs later for deeper submergences because the landslide is initially further downstream, and the initial water surface depression that forms over the landslide has further to travel upstream. An approximate time of occurrence of maximum wave run-down was calculated and compared with the measured values. Wave troughs with lengths of 0.4m, 0.5m and 0.6m, approximately the length of the landslide, were hypothetically generated at various downstream positions and propagated upstream towards the shore. These propagation times for the three different wavelengths are plotted in Figure 12 as a function of initial submergence. The correlation between the measured and calculated times is very good.
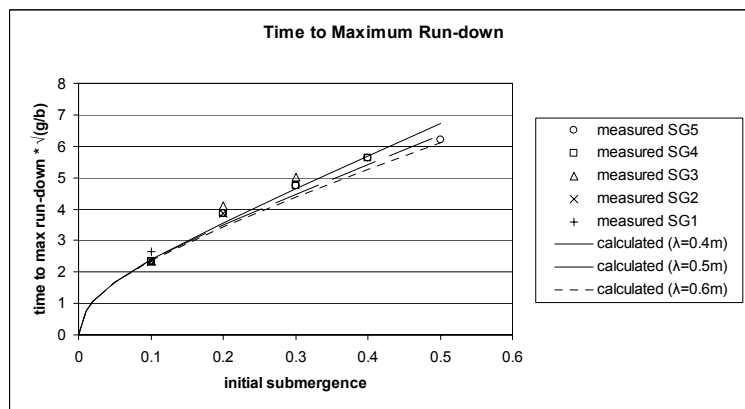

Figure 12. Comparison of measured time of occurrence of maximum wave run-down with calculated values assuming a specific wavelength trough was generated above the initial landslide position and propagated upstream.

3.3 ENERGY

Seismologists use the energy released during an earthquake to quantify the magnitude of the event. Similarly, wave potential energy, landslide potential energy, and landslide kinetic energy are possible measures as to an underwater landslide's potential for destruction. The time histories of the various energy forms also provide insights into the mechanisms in which the energy is transferred from the landslide

potential energy into other forms of energy, such as the wave field. This research appears to be the first experimental tsunami study in which full water surface profile time histories have been generated. The wave potential energy can be determined from this spatial and temporal water level information. Unfortunately it is not practicable to measure the internal kinetic energy of the water motions. The instantaneous potential energy contained in the waves was calculated with equation 3.

$$\text{wave } E_p(t) = \frac{1}{2} \rho_o g w \int_0^\infty \eta(t)^2 \, dx \tag{3}$$

In this expression for wave potential energy, ρ_o is the density of water, g is the acceleration of gravity, w is the width of the flume and landslide, $\eta(t)$ is the water level as a function of time, t, and x is the downstream position. The wave potential energy integration limits were actually between zero and 10.1 m downstream. However, provided waves had not propagated out of our observed domain and the water surface beyond 10.1 m was still, the integration of η^2 between zero and infinity was still valid. The instantaneous landslide kinetic energy was calculated as

$$\text{block } E_k(t) = \frac{1}{2} m_b vel(t)^2 \tag{4}$$

where m_b is the unsubmerged landslide mass and $vel(t)$ is the instantaneous landslide velocity. The instantaneous landslide potential energy is calculated by multiplying the submerged mass of the landslide by the vertical fall distance relative to its initial position, and was calculated as

$$\text{block } E_p(t) = (m_b - m_0)(y(t_0) - y(t)) \tag{5}$$

where m_o is the mass of water displaced by the landslide, $y(t_0)$ and $y(t)$ are the initial and instantaneous vertical position of the landslide respectively.

Figure 13 plots the time histories of wave potential energy, landslide kinetic energy, and the change in landslide potential energy, for the SG3_IS5 test. The key features of this plot are similar for the other combinations of specific gravity and initial submergence. Some of the block potential energy is converted into kinetic energy of the block as it slides down the slope. The remaining potential energy is dissipated as friction on the sliding surface. The motion of the landslide sets in motion some of the surrounding fluid, converting some of the block kinetic energy into kinetic energy of the water. Some of the energy in the water motions is then passed into the wave potential energy, the remainder being dissipated through friction. Note that wave potential energy decreases after approximately 4 seconds due to the propagation of energy out of the observed region. The maximum landslide kinetic energy occurs before the time of maximum landslide potential energy conversion because the block has started to slow before reaching the floor of the flume.
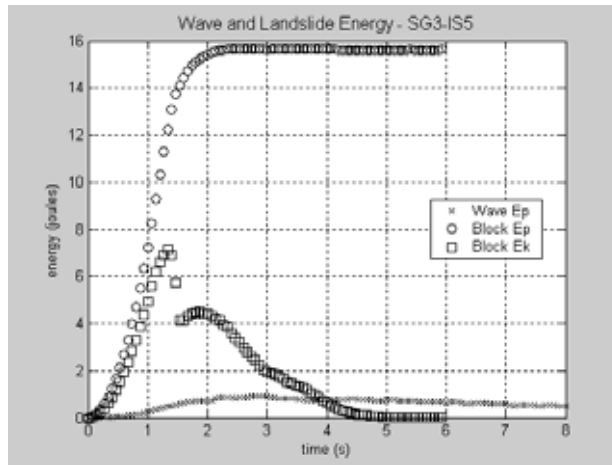
Figure 13. Time histories of wave potential energy (wave Ep), landslide kinetic energy (block Ek), and landslide potential energy converted (block Ep), for the SG3_IS5 test.

The values presented in Figure 14 indicate the maximum conversion of landslide kinetic energy into wave potential energy is between 2.8% and 13.8%. Shallow initial submergences and lighter specific gravities increase the efficiency with which landslide kinetic energy is converted into wave potential energy. Watts (1997) found conversion rates of solid block kinetic energy into wave potential energy of between 3% and 7%. However, his expression for energy conversion was calculated as a function of the landslide terminal velocity and the square of the maximum wave amplitude. The maximum conversion of landslide potential energy into wave potential energy, presented in Figure 14, range between 1.1% and 5.9%, and are greater for shallower initial submergences. The effect of increasing specific gravity is relatively weaker. Weigel (1955) found typical rates of 1-2% for conversion of landslide potential energy into wave potential energy. His wave potential energies were calculated as a function of the sum of the 1st wave trough and 2nd wave crest amplitudes, squared.
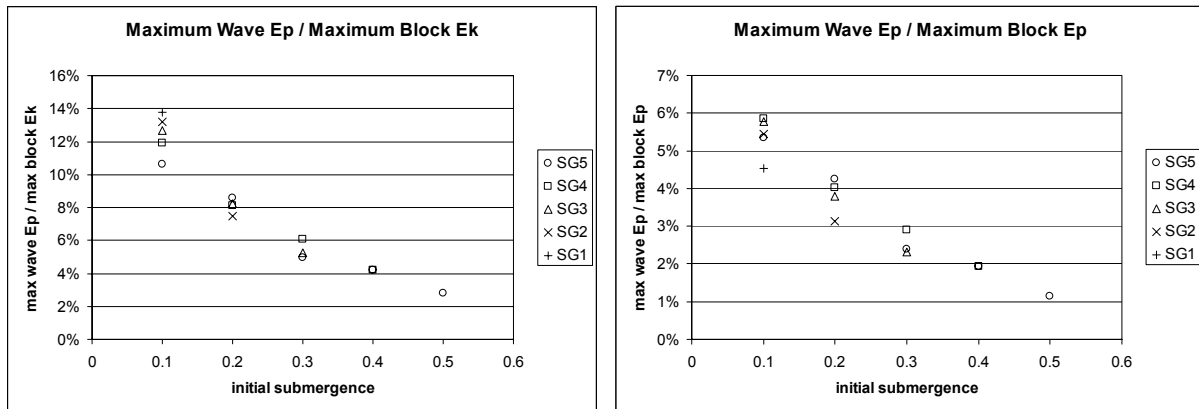

Figure 14. Percentage conversion of maximum landslide kinetic energy into wave potential energy and maximum landslide potential energy into wave potential energy

4. CONCLUSIONS

The focus of this research was to generate underwater landslide-induced tsunami water level data of sufficient quality for comprehensive verification of numerical model results. The experiments carried out here were for a prismatic semi-elliptical block sliding in water 0.435 m deep, along a 15° slope. Techniques utilising PTV and LIF were used to measure the landslide kinematics and water surface profile time histories for fifteen combinations of landslide specific gravity and initial submergence. Rigorous controls were implemented to ensure the repeatability of these tests. The LIF technique developed to measure the spatial and temporal evolution of the water surface was found to produce results with resolution and accuracy comparable to those of traditional electrical point wave gauges.

The measurement of full water surface profile time histories proved advantageous for closely observing and quantifying the initial generation and propagation of laboratory tsunami waves. By comparing the instantaneous position and speed of the landslide relative to the wave field, it was found that the 1st crest formed over the front half of the landslide and a trough formed over the rear. The point at which these two waves met was centred above the landslide centre of mass and remained there as the block slid down the slope.

Wavelengths of individual waves increased as they propagated due to the waves entering deeper water. The dispersion of the waves was evident, as waves further behind in the wave train propagated more slowly than those in front. New waves were continually generated at the trailing end of the wave train. The wave trough initially generated above the rear end of the landslide propagated in both upstream and downstream directions. The upstream-travelling trough was found to cause the large initial draw-down at the shore. The maximum wave run-up height observed at the shore was found to be caused by a wave crest generated by the landslide as it decelerated at the bottom of the slope.

The ability to resolve water levels spatially and temporally allowed wave potential energy time histories to be calculated. Conversion efficiencies for landslide potential energy into wave potential energy ranged from 1.1%-5.9%. Rates for conversion between landslide kinetic energy and wave potential energy ranged between 2.8% and 13.8%.

REFERENCES

Davies, H. L., Davies, J. M., Perembo, R. C. B., and Lus, W. Y. (2003). "The Aitape 1998 tsunami: Reconstructing the event from interviews and field mapping." *Pure and Applied Geophysics*, 160(10-11), 1895-1922.

Enet, F., Grilli, S. T., and Watts, P. "Laboratory Experiments for Tsunamis Generated by Underwater Landslides: Comparison with Numerical Modeling." *Proceedings of the Thirteenth (2003) International Offshore and Polar Engineering Conference, May 25 2003-May 30 2003*, Honolulu, HI, United States, 1717-1724.

Fleming, J. G., Walters, R. A., Sue, L. P., and Nokes, R. I. (2005). "Experimental Design For Solid Block and Granular Submarine Landslides: A Unified Approach." Tsunamis: Case Studies and Recent Developments, K. Satake, ed., Springer, 259-277.

Fritz, H. M., Hager, W. H., and Minor, H. E. (2001). "Lituya Bay Case: Rockslide Impact and Wave Run-up." *Science of Tsunami Hazards*, 19(1), 3-22.

Grilli, S. T., Kirby, J. T., Liu, P. L. F., Brandes, H., and Fryer, G. J. (2003). "Workshop on Model Validation and Benchmarking For Tsunami Generation by Submarine Mass Failure - Proposal Submitted to NSF." Honolulu, Hawaii.

Grilli, S. T., Vogelmann, S., and Watts, P. (2002). "Development of a 3D numerical wave tank for modeling tsunami generation by underwater landslides." *Engineering Analysis with Boundary Elements*, 26(4), 301-313.

Grilli, S. T., and Watts, P. (1999). "Modeling of waves generated by a moving submerged body. Applications to underwater landslides." *Engineering Analysis with Boundary Elements*, 23(8), 645-656.

Imamura, F., and Hashi, K. (2003). "Re-examination of the source mechanism of the 1998 Papua New Guinea earthquake and tsunami." *Pure and Applied Geophysics*, 160(10-11), 2071-2086.

Jiang, L., and Leblond, P. H. (1992). "The Coupling of a Submarine Slide and the Surface-Waves Which It Generates." *Journal of Geophysical Research-Oceans*, 97(C8), 12731-12744.

Kanoglu, U. "Nonlinear Evolution and Runup of a Solitary Wave Over a Sloping Beach." *Long Waves Symposium*, AUTh, Thessaloniki, Greece, 281-288.

Kennedy, A. B., Chen, Q., Kirby, J. T., and Dalrymple, R. A. (2000). "Boussinesq modeling of wave transformation, breaking, end runup. I: 1D." *Journal of Waterway Port Coastal and Ocean Engineering-Asce*, 126(1), 39-47.

Liu, P. L. F., Wu, T. R., Raichlen, F., Synolakis, C. E., and Borrero, J. C. (2005). "Runup and rundown generated by three-dimensional sliding masses." *Journal of Fluid Mechanics*, 536, 107-144.

Lynett, P. J., Borrero, J. C., Liu, P. L. F., and Synolakis, C. E. (2003). "Field survey and numerical simulations: A review of the 1998 Papua New Guinea tsunami." *Pure and Applied Geophysics*, 160(10-11), 2119-2146.

Mariotti, C., and Heinrich, P. (1999). "Modeling of submarine landslides of rock and soil." *International Journal for Numerical and Analytical Methods in Geomechanics*, 23(4), 335-354.

Martel, S. J. (2004). "Mechanics of landslide initiation as a shear fracture phenomenon." *Marine Geology*, 203(3-4), 319-339.

Murty, T. S. (2003). "Tsunami wave height dependence on landslide volume." *Pure and Applied Geophysics*, 160(10-11), 2147-2153.

New Scientist. (2004). "Hawaiian Tsunami Left a Gift at the Foot of Kohala Volcano." *New Scientist*, 2464(2464), 14.

Nokes, R. I. (2005a). "FluidStream v6.01: User's Guide." Christchurch, New Zealand, Particle Tracking Velocimetry (PTV).

Nokes, R. I. (2005b). "ImageStream v5.01: System Theory and Design." Christchurch, New Zealand, Image Processing.

Okal, E. A. (2003). "T waves from the 1998 Papua New Guinea earthquake and its aftershocks: Timing the tsunamigenic slump." *Pure and Applied Geophysics*, 160(10-11), 1843-1863.

Raichlen, F., and Synolakis, C. E. "Run-up From Three-Dimensional Sliding Masses." *Long Waves Symposium*, AUTh, Thessaloniki, Greece, 247-256.

Ruff, L. J. (2003). "Some aspects of energy balance and tsunami generation by earthquakes and landslides." *Pure and Applied Geophysics*, 160(10-11), 2155-2176.

Rzadkiewicz, S. A., Mariotti, C., and Heinrich, P. (1997). "Numerical simulation of submarine landslides and their hydraulic effects." *Journal of Waterway Port Coastal and Ocean Engineering-Asce*, 123(4), 149-157.

Satake, K., and Tanioka, Y. (2003). "The July 1998 Papua New Guinea earthquake: Mechanism and quantification of unusual tsunami generation." *Pure and Applied Geophysics*, 160(10-11), 2087-2118.

Sue, L. P. (in preparation). "Modeling of Tsunami Generated By Underwater Landslides," PhD thesis, University of Canterbury, Christchurch, New Zealand.

Sue, L. P., Nokes, R. I., and Walters, R. (2006). "Modeling of Tsunami Generated By Underwater Landslides." *EQC 6UNI1/506*, University of Canterbury, Christchurch, New Zealand.

Synolakis, C. E. (1987). "The Runup of Solitary Waves." *Journal of Fluid Mechanics*, 185, 523-545.

Tappin, D. R., Watts, P., and Matsumoto, T. (2003). "Architecture and Failure Mechanism of the Offshore Slump Responsible for the 1998 Papua New Guinea Tsunami." Submarine mass movements and their consequences : 1st international symposium, J. Locat and J. Mienert, eds., Kluwer Academic Publishers, Boston, 383-389.

Tappin, D. R., Watts, P., McMurtry, G. M., Lafoy, Y., and Matsumoto, T. (2001). "The Sissano, Papua New Guinea tsunami of July 1998 - offshore evidence on the source mechanism." *Marine Geology*, 175(1-4), 1-23.

Tarman, H. I., and Kanoglu, U. "Numerical Simulation of Long Wave Runup on a Sloping Beach." *Long Waves Symposium*, AUTh, Thessaloniki, Greece, 273-279.

Tinti, S., and Bortolucci, E. (2000). "Energy of water waves induced by submarine landslides." *Pure and Applied Geophysics*, 157(3), 281-318.

Walters, R. "Tsunami Runup: Model Development and Testing." *Long Waves Symposium*, AUTh, Thessaloniki, Greece, 289-296.

Watts, P. (1997). "Water Waves Generated by Underwater Landslides," PhD, California Institute of Technology, Pasadena, California.

Watts, P. (1998). "Wavemaker curves for tsunamis generated by underwater landslides." *Journal of Waterway Port Coastal and Ocean Engineering-Asce*, 124(3), 127-137.

Watts, P. (2000). "Tsunami features of solid block underwater landslides." *Journal of Waterway Port Coastal and Ocean Engineering-Asce*, 126(3), 144-152.

Watts, P., and Grilli, S. T. "Underwater Landslide Shape, Motion, Deformation, and Tsunami Generation." *Proceedings of the Thirteenth (2003) International Offshore and Polar Engineering Conference, May 25 2002-May 30 2003*, Honolulu, HI, United States, 1709-1716.

Watts, P., Imamura, F., Bengston, A., and Grilli, S. T. "Benchmark cases for tsunamis generated by underwater landslides." *Proceedings of the Fourth International Symposium Waves 2001, Sep 2-6 2001*, San Francisco, CA, 1505-1514.

Wiegel, R. L. (1955). "Laboratory studies of gravity waves generated by movement of submerged body." *American Geophysical Union -- Transactions*, 36(5), 759-774.

SAGE CALCULATIONS OF THE TSUNAMI THREAT FROM LA PALMA

Galen Gisler
Los Alamos National Laboratory and University of Oslo
Robert Weaver
Los Alamos National Laboratory,
Michael L. Gittings
Science Applications International
Los Alamos, NM, USA

ABSTRACT

With the LANL multiphysics hydrocode SAGE, we have performed several two-dimensional calculations and one three-dimensional calculation using the full Navier-Stokes equations, of a hypothetical landslide resembling the event posited by Ward and Day (2001), a lateral flank collapse of the Cumbre Vieja Volcano on La Palma that would produce a tsunami. The SAGE code has previously been used to model the Lituya Bay landslide-generated tsunami (Mader & Gittings, 2002), and has also been used to examine tsunami generation by asteroid impacts (Gisler, Weaver, Mader, & Gittings, 2003). This code uses continuous adaptive mesh refinement to focus computing resources where they are needed most, and accurate equations of state for water, air, and rock. We find that while high-amplitude waves are produced that would be highly dangerous to nearby communities (in the Canary Islands, and the shores of Morocco, Spain, and Portugal), the wavelengths and periods of these waves are relatively short, and they will not propagate efficiently over long distances.

1. INTRODUCTION

Tsunami that affect the Atlantic Ocean are much less frequent than those that affect the Pacific and Indian Oceans, nevertheless they do occur. The 1 November 1755 Lisbon earthquake (*e.g.* Chester 2001, Mader 2001) is an example of an event that produced an ocean-wide tsunami. There are other potential tsunamigenic hazards in the Atlantic, including submarine volcanoes (*e.g.* Kick-em Jenny in the Eastern Caribbean, Smith & Shepherd, 1993, 1995), submarine landslides associated with deep ocean trenches and continental slopes, and subaerial landslides, particularly from any of the steep-sided volcanic islands in the Atlantic. Though the frequency of such events is low, the establishment of an Atlantic Tsunami Warning System would be justified for the protection of the millions of people populating Atlantic shores.

This report summarizes the findings of our two-dimensional and three-dimensional simulations of a hypothetical tsunami resulting from the lateral flank collapse of the Cumbre Vieja volcano on the island of La Palma in the Canary Islands. Such a collapse, similar to the Mt St Helens collapse in May 1980, could send as much as 500 cubic kilometers of rock in the form of a debris avalanche into the Atlantic Ocean, triggering a tsunami (Ward and Day 2001). We do not here address the likelihood of such a flank collapse or its eventual magnitude, other than to bracket the magnitude as part of a parameter study we have undertaken. We do note, however, that the Ward and Day work has been met with considerable skepticism in the scientific community. Mader (2001), Pararas-Carayannis (2002), and Wynn and Masson (2003) argue against this, respectively, because a long-period wave is unlikely to result even from a total collapse, because such a total collapse is held to be unlikely, and because the record of turbidite deposits in the vicinity of the Canary Islands does not support such catastrophic events in the past.

Bathymetry of the region around the Canary Islands is essential for the accuracy of this project, and we have requested from the Spanish Government multi-beam bathymetry data that will help resolve the nature and magnitude of the long-range danger from an event of this type. The report presented here is based on the much poorer data available in the public domain. The limited resolution of these data is an important limitation on the quality of the three-dimensional tsunami simulations, and we hope to repeat these calculations when better data become available.

Three-dimensional Navier-Stokes simulations are needed in order to predict the wave radiation pattern that results from a tsunamigenic event. Shallow-water wave theory and other approximations do reasonably well at long-distance propagation given an accurate description of the wave form that results from from an event, but the production of the wave form itself requires accurate calculation of the complex interaction between the water and the perturbing medium. Entrainment, turbulence, and turbidity currents are all important.

While three-dimensions and good bathymetry are needed for calculating the radiation pattern, two-dimensional calculations (depth and longitudinal distance) can predict the wavelengths and periods of the wave trains that are produced from the triggering event, while greatly overestimating amplitudes. Since two-dimensional calculations are relatively inexpensive and can be done at high resolution, parameter studies work well to determine how the observed characteristics of the wave depend on the physical inputs of the event.

2. THE SAGE HYDROCODE

The SAGE hydrocode is a multi-material adaptive-grid Eulerian code with a high-resolution Godunov scheme originally developed by Michael Gittings for Science Applications International (SAIC) and Los Alamos National Laboratory (LANL) under the Department of Energy's program in Advanced Simulation and Computing, or ASC. It solves the full set of compressible Navier-Stokes equations, and uses continuous adaptive mesh refinement (CAMR), by which we mean that the decision to refine the grid is made for each cell at every cycle throughout the problem run, depending on gradients in physical properties. With this technique, large computational volumes with substantial differences in scale can be simulated at low cost.

Each cell in the computational volume can contain all materials defined in the problem with different equations of state and rheology. We use the LANL SESAME tables of material properties for air and basalt, but for water we used a more sophisticated table that includes a good treatment of the vapor dome and phase transitions from SAIC. Detailed testing of the water equation of state shows excellent agreement with experimental results.

The boundary conditions we use in these tsunami calculations are designed to allow unhindered outflow of waves and material. This is accomplished by the use of "freeze regions" around the edges of the computational box, which are updated normally during the hydrodynamic step, then quietly restored to their initial values of pressure, density, internal energy, and material properties before the next step. This technique has proven to be extremely effective at minimizing the deleterious effects of artificial reflections.

3. TWO-DIMENSIONAL SIMULATIONS OF CHARACTERISTIC SUBAERIAL LANDSLIDES

A simple schematic slide geometry was suggested to us by Simon Day (private communication) as a two-dimensional representation of likely slides at Cumbre Vieja. The slide region is wedge shaped, deepest at the top, tapering to a point or toe at the bottom, and having an offset towards the back (east) side of the peak (see Figure 1). Below this, to the bottom of the computational grid, is a rigid reflecting boundary representing the unchanging basement rock of La Palma. The motion is initiated solely by the gravitational acceleration of the fluidized rock (with the density of basalt) in the slide region. The two-dimensional calculations are done in Cartesian coordinates, thus effectively assuming infinite extent in the direction perpendicular to the simulation plane.
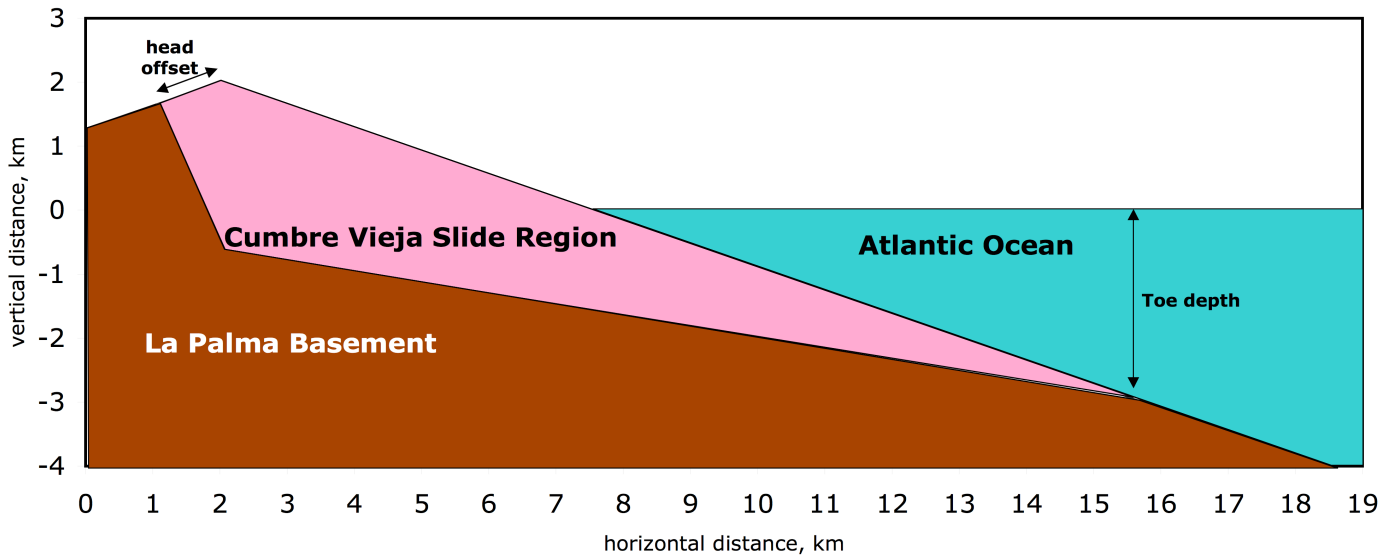
Figure 1. Schematic setup for our two-dimensional runs. The pink material labeled "Cumbre Vieja Slide Region" is the fluidized rock that accelerates under gravity and slides down into the ocean (blue). The brown region labeled "La Palma Basement" is an internal reflective boundary. The setup shown here is for run Dth31, with toe depth 3 km and head offset 1 km. Varying these two numbers constituted our parameter study.

We ran four variants of this geometry, with the toe at depths of 2 and 3 kilometers, and the head offset at 1 and 2 kilometers. These runs are named so as to indicate the toe depth and head offset; thus Dth21 has toe depth 2 km and head offset 1 km, and Dth32 has toe depth 3 km and head offset 2 km. The total volumes, assuming a 25 kilometer perpendicular extent are: run Dth21, 308 km^3; run Dth22, 332 km^3; run Dth31, 473 km^3; and run Dth32, 503 km^3. These are all run with a finest resolution of 15 meters, certainly adequate to resolve the (hundreds of meters) initial wave heights expected. This resolution also enables the tracking of turbidity currents as the fluidized basalt slide material mixes with the water, and can help diagnose the energy trades that occur between the slide material and the water, and between the water and the atmosphere. These runs have on the order of 300,000 cells, and ran for a few hundred hours on 10–20 processors of a Linux Opteron cluster at Los Alamos.

An impression of the character of the wave is obtained from a graphic rendering of density at a time early in the calculation (Fig. 2). This figure shows a small portion of the computational domain; the box extends to the right out to a distance of 120 km from the island. The fluidized rock has accelerated into the water, initially producing a crater, then a substantial wave. The slide speed in this inviscid calculation reaches as high as 190 m/s before decelerating as the slide gives up energy to the water. The peak slide speed almost matches the shallow-water wave speed ($\sqrt{gd} \sim 198$ m/s) so the bullnose of the slide material falls behind the water wave only gradually, and continues to pump energy into the water wave. A single broad wave is thus produced, with trailing higher-frequency components that are excited by the eddy currents in the turbulent mixing and entrainment of slide material and water. As the slide material decelerates, the water wave detaches and outruns

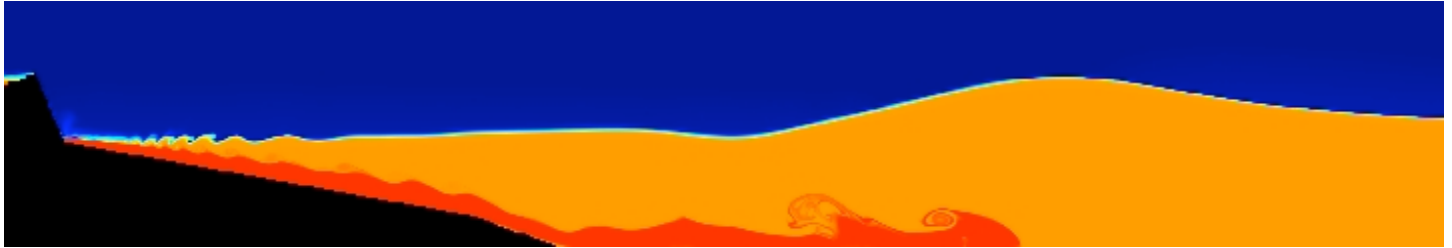it, but no further low-frequency modes are produced.

Figure 2. Density raster plot in our 2d run Dth32 at a time of 180 seconds after the start of the slide. The reflective region representing the unchanging basement of La Palma is at left in black, the basalt fluid slide material is red, water is orange, and air is blue. Intermediate shades represent the mixing of fluids, in particular the turbidity currents mixing water and basalt are readily apparent. The water wave leads the bullnose of the slide material by a small amount; the forward-rushing slide material (with a velocity of 190 meters/second almost matching the wave velocity) continues to pump energy into the wave. The wave height at this time is 1500 meters, and the wavelength is roughly 60 km. This figure has a width of 50 km, representing less than half of the computational domain, which extends 120 km to the right.

We measured maximum wave heights, wavelengths, periods, and wave speeds for these four runs, and summarize them in Table I. These quantities were obtained by inspecting the trajectories of massless Lagrangian racer particles initially placed along the surface of the water. Graphs of vertical (y) and horizontal (x) position as functions of time for the tracers in run Dth32 are presented in Figure 3.

Table I. Important characteristics of the two-dimensional runs

run	slide volume (km^3)	max wave height (m)	wavelength (km)	period (s)	wave speed (m/s)
Dth21	308	1303	48	252	192
Dth22	332	1327	48	250	192
Dth31	473	1474	53	262	202
Dth32	503	1508	61	291	209

The wave period and wavelength depend only weakly on the slide volume (roughly as the 1/3 and 1/2 power, respectively), but both the period and wavelength of these waves are short compared to those of teletsunamis commonly observed in the Pacific or Indian Ocean. The long-distance propagation of these waves will not be as effective as classical long-wavelength tsunamis. We do not see low-frequency components arising in the water wave, though a cascade to higher frequency is apparent in the tracer plots of Figure 3. Concerned that our 120 km box length prevented the development of lower frequency waves, we repeated the Dth31 calculation with a box length of 240 km, producing results that were identical in all respects.
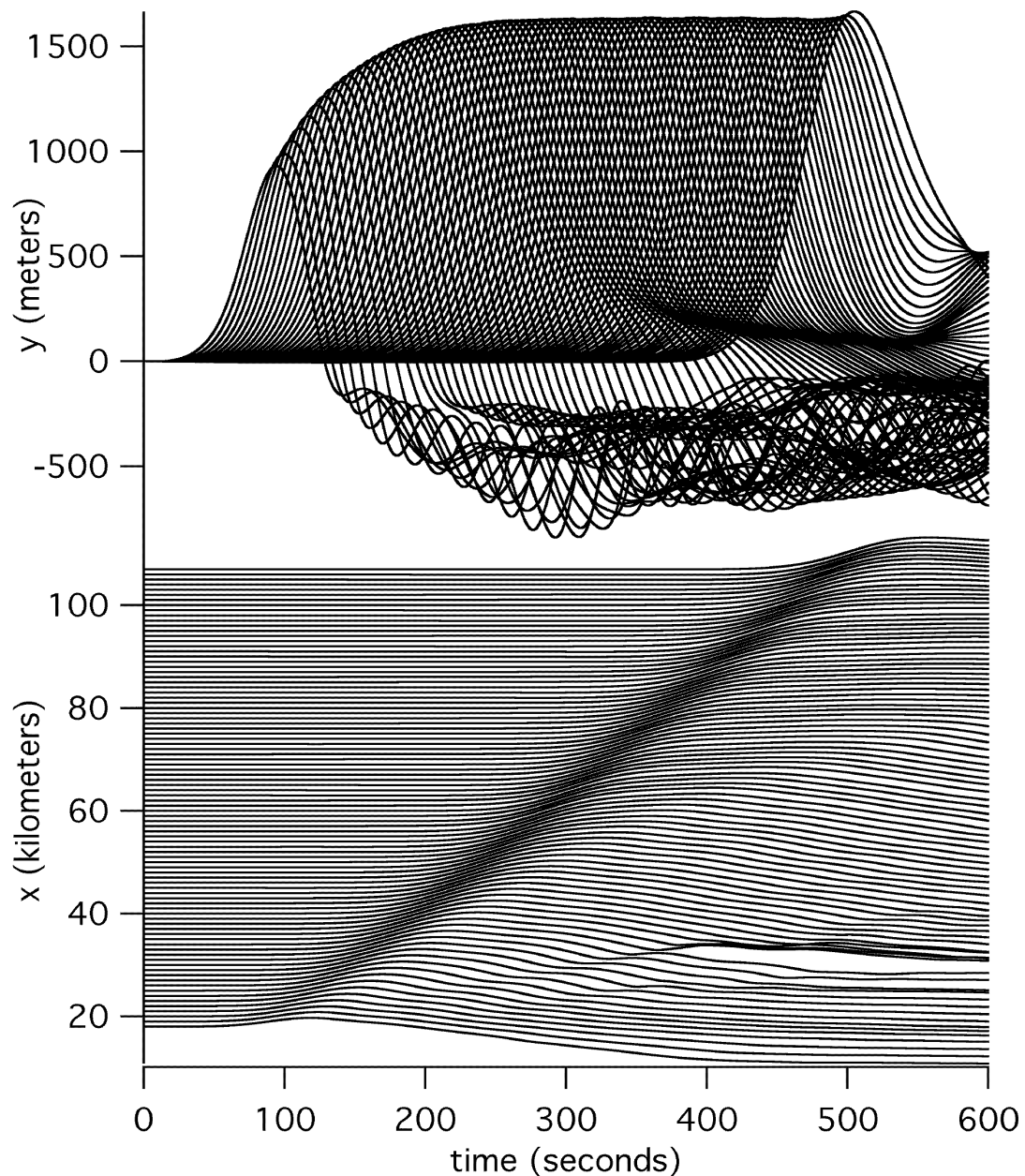
Figure 3. Tracer positions as a function of time in run Dth32. Top is vertical position, bottom is horizontal position. The wave velocity is measured directly from the bottom plot, and amplitude and period are estimated from the upper plot. Although the massless Lagrangian tracers are placed initially on the water surface, they do not remain on the surface but follow the fluid in the computational cell in which they happen to reside at any given time. Therefore they tend to random-walk away from the surface into the body of the water. This accounts for the late-time under-surface tangle in the top plot towards late time.

It is very important to note that although these waves probably do not pose a significant danger to the western shores of the Atlantic Ocean, these large-amplitude waves will be very dangerous locally, *i.e.* to the

shores of other islands in the Canaries Archipelago and to mainland Africa and Europe.

For validation of the periods and wavelengths determined by SAGE, we turn to the example of the Ritter Island tsunami in Papua New Guinea in 1888, which was triggered by a debris avalanche following the eruption of the Ritter Island volcano (Ward and Day 2003). The geometry and mechanism are similar to those of the hypothetical La Palma event, but the slide cross-section is considerably smaller. We ran a calculation of Ritter Island with SAGE, and found a wave period of 180s, in agreement with the observations made at the time, see Figure 4 for the tracer plots. This period also accords with the 1/3-power volume scaling from the La Palma parameter study as mentioned above.
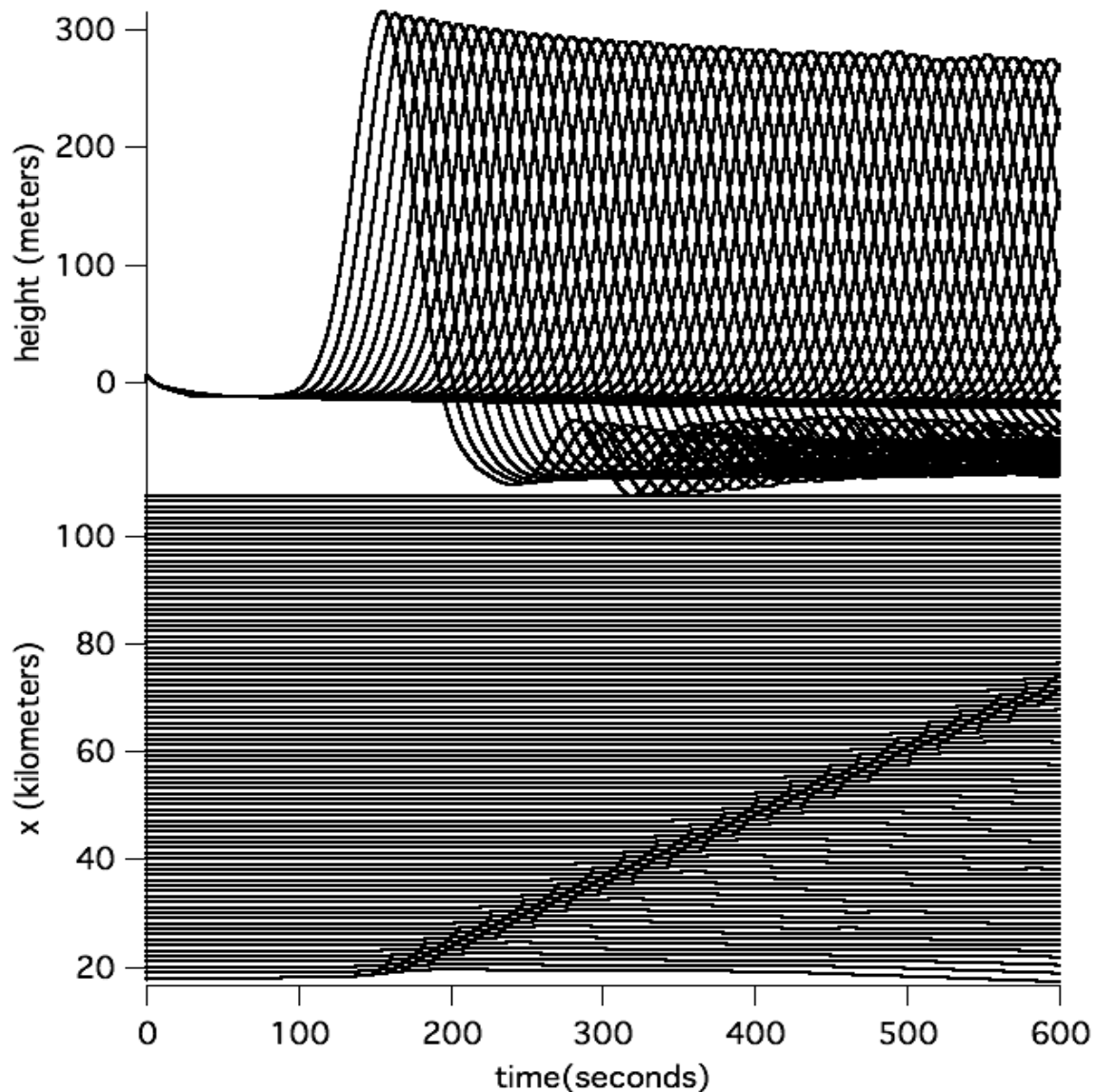

Figure 4. Tracer positions as a function of time in our Ritter Island simulation run. As in Figure 3, top is vertical position, bottom is horizontal position. The wave velocity is measured directly from the bottom plot, and amplitude and period are estimated from the upper plot.

Because the basalt slide is treated as an inviscid fluid in the calculations reported above, the speed and eventual reach of the slide material may be overestimated. To judge this, we preformed an additional set of calculations treating the rock slide as a plastic flow, with a shear modulus of 1 kBar and nominal yield stress, so that flow begins immediately. In Figure 5 we show comparisons of our Dth31 run with the plastic flow run Gth31, which is otherwise identical. We find that the slide is considerably slower in the plastic flow case. At 270 seconds, the time of the figure, the Dth31 slide has a horizontal velocity of 148 m/s, while the Gth31 slide has 131 m/s. Since these speeds are still possibly higher than expected, it may be that the plastic flow model would require a greater shear modulus to be realistic.
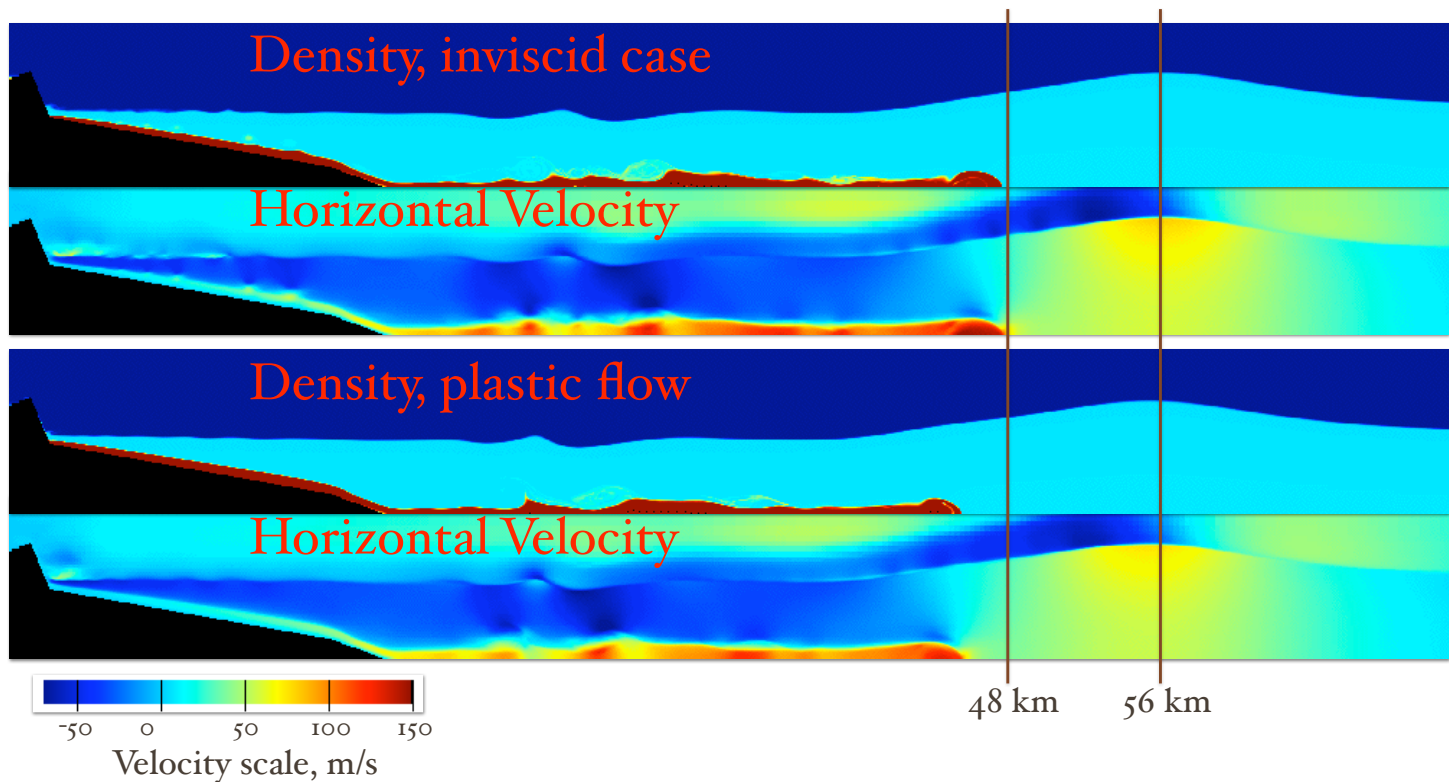

Figure 5. Comparison of the inviscid-slide calculation Dth31 with the plastic-flow slide calculation Gth31 at 270 seconds after the start of the calculation. The slide in Gth31 is significantly retarded in velocity and position with respect to the inviscid case, and the ripples in the basalt slide (which would represent turbidite layerings) are further apart and suppressed in amplitude. The maximum horizontal velocity of the slide material is 150 m/s in the inviscid case, 130 m/s in the plastic-flow case. The position and velocity of the water wave are unaffected. Note the strong velocity gradient across the water-air interface at and behind the wave crest in both cases. The Kelvin-Helmholtz instability will very likely cause the wave to degenerate further into high-frequency components. The amplitude of the wave in Gth31 is also very slightly less than in Dth31.

However, some landslides are well known to be quite runny, and may be lubricated by fragmentation and melt in the lower layers, or by acoustic fluidization as in sturzstroms (Collins and Melosh, 2003). Studies are underway to establish a good validation point. More relevant to observations of past landslides is the fact that

the plastic flow case produces larger eddies, and hence larger intervals between turbidite layers in the same landslide. Studies of turbidite layers in Hawaiian and Canary Island landslides (Wynn and Masson 2003) as well as for truly massive events such as Storegga, may prove useful for helping to untangle underwater slide dynamics. The position and speed of the water wave are the same in both calculations, but the amplitude is slightly less in the case with the debris avalanche treated as a plastic flow (1462 meters as compared with 1532 meters).

4. THREE-DIMENSIONAL SIMULATIONS OF A LA PALMA/CUMBRE VIEJA LANDSLIDE

The very high amplitudes found in our two-dimensional calculations are in the first place suspect because the Cartesian calculation geometry does not allow for dispersion in the transverse direction. A simple and inexpensive way to estimate the effect of transverse dispersion is by running a similar calculation in cylindrical coordinates, then this can further be checked by running a full three-dimensional calculation.

By way of illustration, then, we present in Figure 6 tracer particle plots for the two-dimensional Cartesian D31 and a two-dimensional cylindrical run with similar parameters. The maximum wave height is down by a factor 3, and the amplitude declines with distance from the source roughly as r^{-1} as expected.
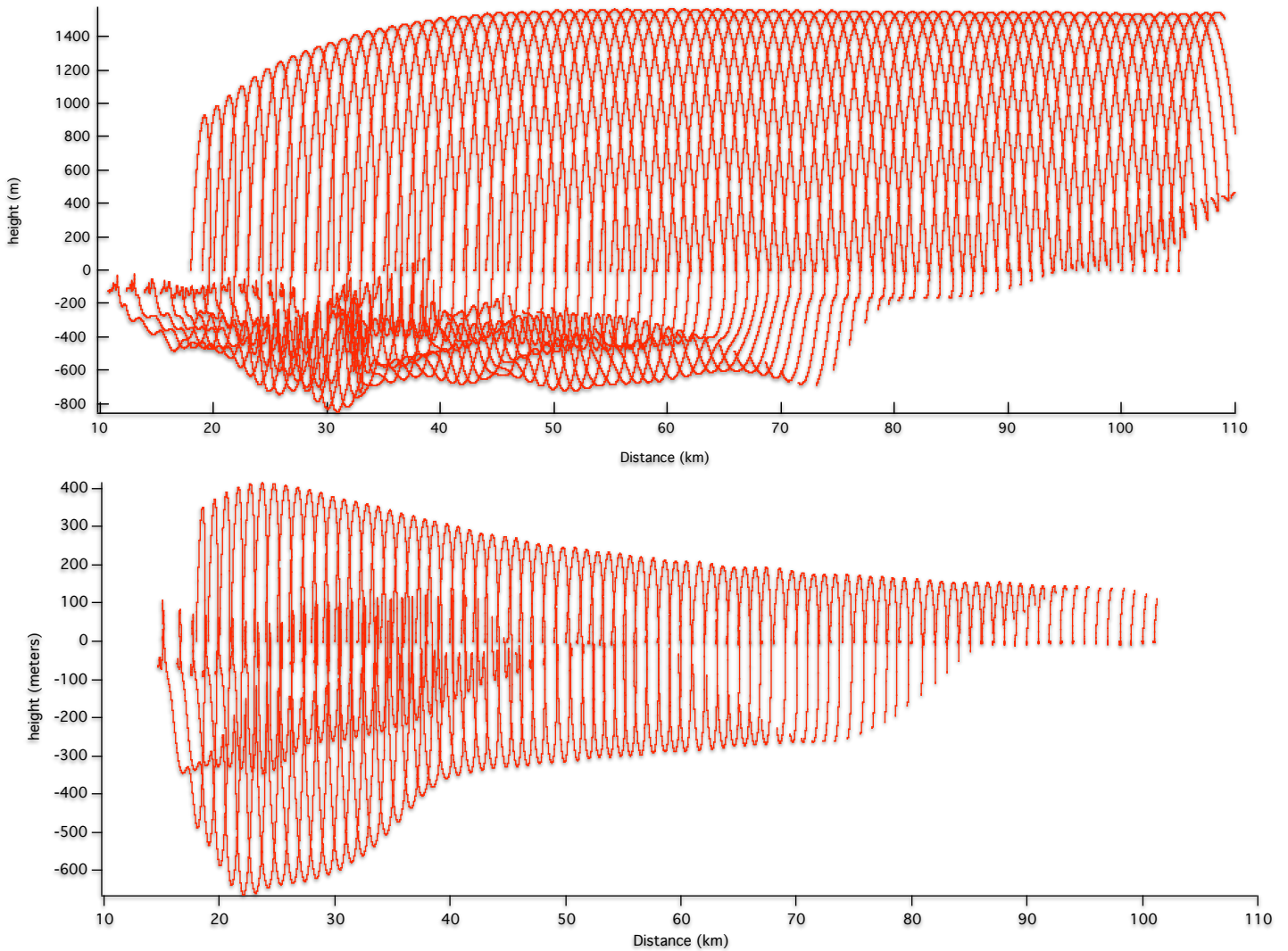
Figure 6. Comparison of tracer particle trajectories in the vertical plane for the Cartesian-geometry calculation Dth31 and the cylindrical-geometry-calculation Cth31. The maximum amplitude is less by a factor 3 in the latter case, and the expected r^{-1} decline with distance away from the source is observed.

Our single three-dimensional run of the hypothetical La Palma landslide uses publicly available bathymetry and topography from the web site of the USGS. Because the resolution of these data is so coarse (2 minutes, or roughly 4 kilometers), we've chosen much coarser resolution for this run, namely 125 meters. The slide region for this run was made by performing rather simple geometrical cuts on the crude topography to yield a volume in the range considered by Ward and Day, with no reference to actual geological features of the Cumbre Vieja volcano. Our slide has a volume of 375 km^3. This run has on order 60,000,000 cells, and requires 500 processors of a Linux Xeon cluster at Los Alamos. Because of the coarse resolution, we have so far used this run only to make a first pass at the radiation pattern of the tsunami that would result from the proposed slide. This radiation pattern, at a time of 209 seconds after the start of the gravity-initiated slide, is shown in Figure 7.
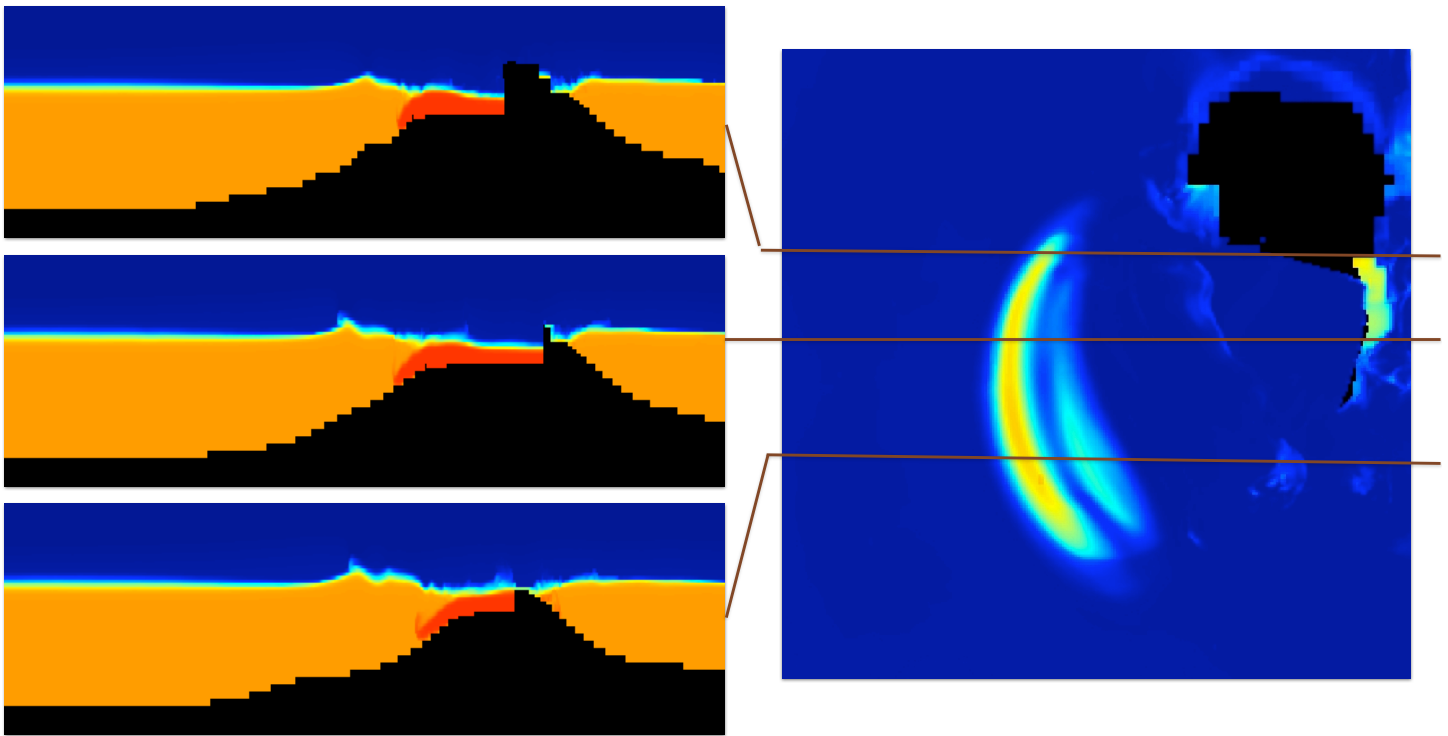
Figure 7. At right, a density raster plot in a horizontal slice through our 3d calculation at 500 meters altitude at a time of 209 seconds, and at left, three vertical slices through the same calculation at the positions indicated. The reflective region representing the island of La Palma is in black, and the original slide position has been vacated. Deep blue represents the density of air, orange the density of water, and shades in between indicate mixtures of air and water. The peak of the large-amplitude wave is directed towards the SSW, and a following crest is following in the same direction. A line extended through the peak strikes the northeast coast of South America. The vertical slices at left (exaggerated 5 times in the vertical direction) show that the highest wave is at the southern end of the slide. With more accurate bathymetry, we should be able to provide a fairly good prediction of the full radiation pattern. Note that there is considerable wave energy at this 500 meter level directed towards the other islands in the Canaries archipelago and toward the African and Spanish mainland, indicating the possibility of locally dangerous waves impinging on those shores.

In this three-dimensional run we find that the wave has even a shorter wavelength than we saw in the two-dimensional runs, but we await the high-quality bathymetry from the Spanish government before committing to this interpretation and evaluating quantitatively the threat to North America. It seems clear, nevertheless, that there is no significant wave energy directed towards the North Atlantic. If there is a long-distance threat from an event of this type, the regions most likely to be affected would be the Eastern Caribbean and the Northeastern Coast of South America. Considerable damage would be expected, however, in the Canaries, Morocco, Portugal and Spain if a large-scale collapse of Cumbre Vieja were to occur.

We make an attempt to estimate the distant effects by using the maximum height of the waves detected by our Lagrangian tracer particles as a function of distance from the source in our admittedly crude three-dimensional simulation. These simulation data are shown in Figure 8, which suggests a considerably stronger decline with distance than the r^{-1} decline seen in the cylindrically-symmetric run. The reasons for this difference may have to do with more degrees of freedom for the air/water and rock/water interaction instabilities, but the

coarseness of the resolution used in the three-dimensional calculation may also be a factor. In any case, we may use the r^{-1} decline seen in the cylindrical-geometry run and the $r^{-1.85}$ decline seen in the three-dimensional run to bracket extrapolations of the wave amplitudes expected in Surinam (towards which the strongest waves are evidently headed, from Figure 7) and Florida. For Surinam, at a distance of 4700 km from La Palma, the r^{-1} decline yields a wave height of about a meter, and the $r^{-1.85}$ decline yields a wave height of only about 2 cm. For Florida, at a distance of 6100 km, the r^{-1} decline yields a wave height of about 77 cm, and the $r^{-1.85}$ decline yields a wave height of only about 1.2 cm. Even the largest of these estimates is considerably smaller than the worrisome values given by Ward and Day (2001). Shoaling and distant focusing are of course omitted here, but are not expected to yield disastrous waves in any case.
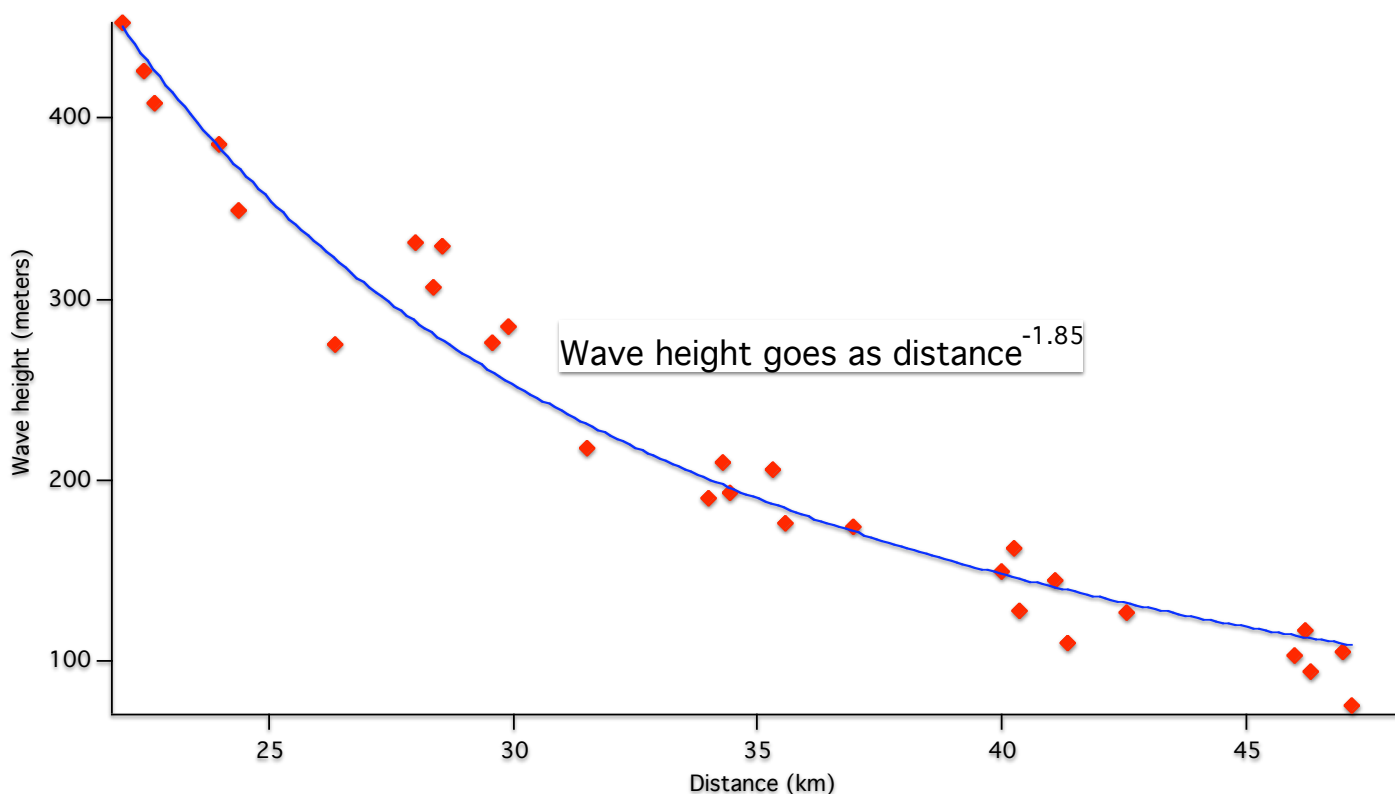

Figure 8. Maximum wave heights detected by our Lagrangian tracer particles as a function of distance away from the initial landslide peak, together with a best-fit power-law line giving a decline with distance as $r^{-1.85}$. If the long-distance wave propagation continues to decline in this way, the waves expected on the western shores of the Atlantic Ocean are unimportant.

5. FUTURE WORK

We intend to undertake new calculations in three dimensions of this scenario which will utilize the better bathymetric data of the Canary Islands furnished by the Spanish government. We have also enlisted the assistance of a group at Stanford University who have an incompressible flow solver together with a granular flow treatment for physics of the landslide itself. Granular flow and landslides are also a subject of intense

interest at the Centre for the Physics of Geological Processes at the University of Oslo, where one of us (Gisler) has recently moved, and are done there with finite-element and special-purpose methods focusing on fragmentation and lubrication effects. These calculations will complement the pure fluid, fully compressible solver in SAGE. Compressible-flow effects are indeed highly relevant in the very early stages of tsunami generation; but runs to longer physical times are more easily done with an incompressible solver, giving smooth transitions to the long-distance calculations done by tsunami propagation codes.

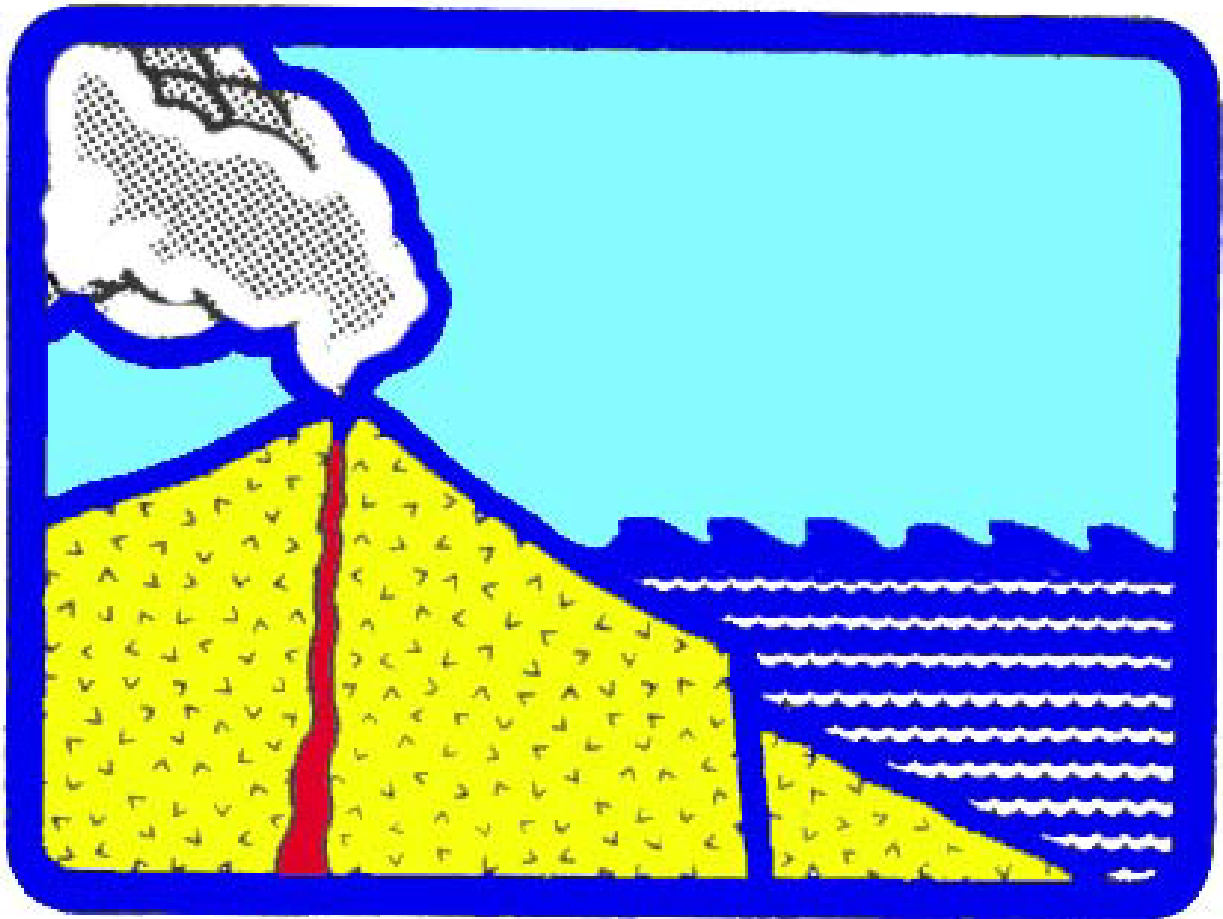## REFERENCES

D. K. Chester, "The 1755 Lisbon earthquake", *Progress in Physical Geography,* **25**, 363-383, 2001.

Gareth S. Collins & H. Jay Melosh, "Acoustic fluidization and the extraordinary mobility of sturzstroms", *Journal of Geophysical Research*, **108** (B10), 2473 doi:10.1029/2003JB002465, 2003.

Galen Gisler, Robert Weaver, Charles Mader, & Michael Gittings, "Two- and Three-Dimensional simulations of asteroid ocean impacts", *Science of Tsunami Hazards*, **21**, 119, 2003.

Charles L. Mader & Michael L. Gittings, "Modeling the 1958 Lituya Bay mega msunami, II", *Science of Tsunami Hazards*, **20**, 241, 2002.

Charles L. Mader, "Modeling the 1755 Lisbon tsunami", *Science of Tsunami Hazards*, **19**, 93, 2001.

Charles L. Mader, "Modeling the La Palma landslide tsunami", *Science of Tsunami Hazards*, **19**, 160, 2001.

M. S. Smith & J. B. Shepherd, "Potential Cauchy-Poisson waves generated by submarine eruptions of Kick 'em Jenny volcano", *Natural Hazards* **11**, 75-94, 1995.

George Pararas-Carayannis, "Evaluation of the threat of mega tsunamis generation from postulated massive slope failures of island stratovolcanoes on La Palma, Canary Islands, and on the island of Hawaii", *Science of Tsunami Hazards*, **20**, 251, 2002.

M. S. Smith & J. B. Shepherd, "Preliminary investigations of the tsunami hazard of Kick 'em Jenny submarine volcano", *Natural Hazards* **7**, 257-277, 1993.

Steven N. Ward & Simon Day, "Cumbre Vieja Volcano — potential collapse and tsunami at La Palma, Canary

Islands", *Geophysical Research Letters* **28**, 397-400, 2001.

Steven N. Ward & Simon Day, "Ritter Island Volcano — lateral collapse and the tsunami of 1888", *Geophysical Journal International*, **154**, 891-902, 2003.

R. B. Wynn & D. G. Masson, "Canary Island landslides and tsunami generation: can we use turbidite deposits to interpret lansdlide processes?" pp325-332 in: *Submarine Mass Movements and their Consequences* (eds. J. Locat and J. Mienert). Kluwer Academic Publishers, Dordrecht, Boston, London, 2003.